Journal of Structural Geology 167 (2023) 104778

Contents lists available at ScienceDirect

Journal of Structural Geology

journal homepage: www.elsevier.com/locate/jsg

Modeling of dike-induced graben nucleation in the Elysium region, Mars: The role of planetary gravity

Sam Rivas-Dorado *, Javier Ruíz, Ignacio Romeo

Departamento de Geodinámica, Estratigrafía y Paleontología, Universidad Complutense de Madrid, C/ Jose Antonio Novais, 12, 28040, Madrid, Spain

ARTICLE INFO

Keywords:
Dikes
Graben
Mars
Models

ABSTRACT

We have studied the processes of dike-induced graben nucleation through the analytical modeling of the failure sequence, i.e., the timing, location, and mode, of the discontinuities formed between the dike's upper tip and the surface. To this end we use as input parameters dike geometry and the elastic and frictional properties of a homogeneous medium. We applied this analytical model to three dike-induced graben in the Elysium region of Mars; Galaxias, Elysium, and Cerberus Fossae, some of which have been found to show active extensional tectonics. Firstly, we calculated dike aperture and depth from graben topography using an area balance technique. At each site we modeled with different combinations of input parameters which resulted in a total 27 models, of which 14 were found to be compatible with the inferred present-day graben-bounding faults. Based on these results we propose two conceptual models of dike-induced graben nucleation: 1) in a shallow dike intruding a low-compliance host rock, nucleation occurs through the linkage of near-surface mode I cracks and mode II discontinuities propagated from the dike tip, and 2) in a deep dike intruding a stiff host rock, shallow mode I cracks propagate to depth and collapse into normal faults in a dominantly tensile regime. A comparison of equivalent models under Martian versus Terrestrial conditions shows that in the former case failure is more likely to occur in a tension-dominated regime due to the greater weight of the dike induced stresses in a medium with a reduced lithostatic load. On Mars, dense networks of open fractures may have facilitated large fissure eruptions. On Earth, tensile failure occurs at very shallow depths whilst faults accommodate most of the deformation at depth. Our analytical modeling methodology explains intrusion experiments and observed dike-induced deformation. Therefore, the models provide plausible mechanisms of graben nucleation above intruding dikes. These need to be complemented by models which simulate long-term graben subsidence above dikes, which may be key to understand seismicity in tectonomagmatically active regions of Mars.

1. Introduction

1.1. Background and scope of work

Long narrow graben throughout the surface of Mars, which are especially abundant in the vicinity of the two volcanic provinces of Tharsis and Elysium, have long been hypothesized to be the result of dike intrusions. Giant water outflows linked to many of these graben systems, such as the Elysium-Utopia flows (Russell, 2003), or Athabasca Valles and Cerberus Fossae (Burr et al., 2002; Head et al., 2003; W. L. Jaeger et al., 2007; Cassanelli and Head, 2018) have been proposed to be the result of catastrophic interactions between the propagating dikes and a shallow cryosphere (McKenzie and Nimmo, 1999). These putative dike-induced structures provide an excellent opportunity for testing the conditions, including the role of gravity, under which dike-related graben nucleation may occur.

The early numerical models of deformation and stresses induced by opening cracks (Pollard et al., 1983; Pollard and Segall, 1987; Rubin and Pollard, 1987) were first tested against scaled laboratory experiments (Mastin and Pollard, 1988) and measurements of terrestrial dike-induced subsidence (Rubin and Pollard, 1988; Rubin, 1992). The models showed that crack-related displacements produce a characteristic topography at surface: upward displacement to the sides of the dike and downward above it. This closely resembled the geodetic record of ground subsidence caused by diking episodes in Iceland and Ethiopia (Rubin and Pollard, 1988).

These early works established a solid linkage between dike intrusion and surface subsidence, and thus graben formation, and their results

* Corresponding author.
E-mail address: samuelrivas@ucm.es (S. Rivas-Dorado).

https://doi.org/10.1016/j.jsg.2022.104778
Received 7 June 2022; Received in revised form 19 December 2022; Accepted 20 December 2022
Available online 29 December 2022

were soon applied to Lunar and Martian graben. Head and Wilson (1992, 1993) and Mège and Masson (1996) used simple relationships between graben width-top dike depth and graben depth-dike aperture to approximate the dimensions of presumed dikes underneath long linear graben in both planetary bodies. In a similar way, Scott (2002) used the ratios in Rubin (1992) to calculate top dike depths and apertures from graben parameters. Later numerical models by Wilson and Head (2002) took the reverse approach. They calculated plausible dike apertures by considering host rock and magma densities, compensation depths and regional tensile stresses, and used the various graben-dike ratios in Rubin (1992) to invert graben dimensions. Interestingly, they obtained graben sizes consistent with topography revealed by the MOLA instrument (Mars Orbiter Laser Altimeter). Schultz et al. (2004) and Goudy and Schultz (2005), similarly to Rubin and Pollard (1988), calculated the theoretical dike-induced displacements and compared them with MOLA-derived topography of multiple graben in Mnemonia Fossae and Arsia Mons, finding very good agreement between the two. Recently, Rivas-Dorado et al. (2021) calculated proxy dike apertures and depths through cross-section balancing of grabens in Elysium Fossae, and obtained dike aspect ratios (length-aperture) which were consistent with those expected for fluid-induced fractures.

Therefore, there is reasonable evidence to support that long and narrow linear graben on Mars host dikes at depth. However, relatively little work has been done to understand the mechanisms leading to dike-induced graben nucleation, in both Martian and terrestrial settings. Some attempts to understand these processes have been experiments of brittle deformation in granular media. In laboratory experiments by Mastin and Pollard (1988), tensile fractures were formed at the surface and ahead of the dike tip which transformed into high-angle dip-slip faults at depth. More recent discrete element models (DEM) by Hardy (2016) simulated dikes between 100 and 600 m thick at depths between 1.3 and 3.3 km. These resulted in discrete shear zones accumulating most of the extension above the dike, leading to the nucleation of ≈60° normal faults at surface. Trippannera et al. (2014, 2016) created experiments with a similar setup to those in Mastin and Pollard (1988), in which they obtained various styles of faulting for thickening dikes as a function of depth and dike tip geometry. Through a DEM method based on spring-connected elements, Koehn et al. (2019) created dynamic models of dikes with thicknesses up to 20 m at 200–1000 m depth, and obtained complex arrays of zigzagging faults which produced subvertical scarps at surface and higher dip angle faults at depth.

Thus, although all models resulted in the formation of broadly similar features (i.e., joints and/or normal faults and generalized subsidence), their sequences of events vary, and the exact structures modeled are different. Generalized explanations for the processes occurring and the discontinuities forming between the dike tip and the surface, based on fundamental principles of fracture and rock mechanics, which can be generally applied to any planetary body, are relevant to understanding dike-related failure but are still missing. Diking is a critical contributor to the accommodation of deformation in volcanic regions, from divergent margins to island arcs, (e.g., Ebinger and Casey, 2001), and recent episodes have put forward its relevance as a graben-nucleating mechanism. Events such as the Bardarbunga-Holuhraun dike (Iceland, 2014, e.g., Sigmundsson et al., 2015), the first event in the Manda-Hararo sequence (Ethiopia, 2005, e.g., Ayele et al., 2009), or the Harrat-Lunnayir intrusion (Saudi Arabia, 2009, e.g. (Pallister et al., 2010), have all seen the formation of shallow incipient graben. On Mars, deep fully evolved dike-induced graben may be related to giant floods, recent volcanism, and even seismicity (Rivas-Dorado et al., 2022). Diking includes the creation of complex arrays of structures which evolve over different timescales and therefore, developing a solid theory of dike-induced failure is key to understanding their role in the geodynamics of rocky planets.

In this work we present complete models of the timing, location and modes of the discontinuities formed during the early stages of diking and apply them at three sites in the Elysium volcanic province, in which narrow graben are hypothesized to be underlain by dikes at depth. From our results we propose two conceptual models of dike-induced graben nucleation on Mars. To provide a more complete picture of these processes, we modeled equivalent dikes in terrestrial and Martian conditions and propose general differences between dike deformation styles in both settings. Our methodology allows to explain the results of many laboratory experiments and field observations, which supports its consistency.

1.2. Areas of study

We selected three long linear graben surrounding the Elysium volcanic bulge with a WNW-ESE constant strike: Galaxias Fossae (GF), Elysium Fossae (EF) and Cerberus Fossae (CF) (Fig. 1a, b, c, d). Galaxias Fossae is located approximately 900 km northwest of Elysium Mons and consists of one main WNW-ESE graben 380 km long (Fig. 1b), which cross-cuts Amazonian volcanics and mid Amazonian lowland units (Tanaka et al., 2014). Therefore, Galaxias Fossae should be expected to be relatively young. Interestingly, many narrow ridges with a more northerly orientation located SW of this structure have been previously identified as exposed dikes (Pedersen et al., 2010). Elysium Fossae is a long multi-graben system of approximately 350 km length located in the eastern flank of Elysium, and is completely embedded in Amazonian volcanics (Tanaka et al., 1992, 2014). The selected graben corresponds to one of the most proximal fossi to the volcano and is the longest structure which can be continually mapped (Fig. 1c). Ages of lava flows around Elysium Fossae are between 1 and 3 Ga (Platz and Michael, 2011; Pasckert et al., 2012), which gives a wide range of possible ages for the graben system. Finally, CF is located some 1200 km SE of Elysium and consists of several graben of up to 150 km length which cross-cut ancient Hesperian-Noachian basement, Amazonian-Hesperian volcanics, and low-lying Amazonian volcanics and volcanoclastic units (Tanaka et al., 2014). Interestingly, Cerberus Fossae is the site of recently detected marsquakes (e.g., Giardini et al., 2020; Brinkman et al., 2021; Knapmeyer-Endrun et al., 2021). The selected graben corresponds to one of the central structures (Fig. 1d), which cross-cuts both Hesperian-Noachian basement and lower Amazonian volcanics. These structures cross-cut terrains as young as Late Amazonian (i.e., <0.6 Ga) and thus they are extremely young features, in accordance with the history of recent volcanism in the Elysium province, in which volcanic activity has been dated to be as modern as <222 ky (Roberts et al., 2007; Vaucher et al., 2009; Jaeger et al., 2010; Pasckert et al., 2012; Andrews-Hanna, 2017; Horvath et al., 2021).

2. Methodology

2.1. Dataset

For each location we retrieved MOLA PEDR (Precision Experiment Data Record) (Smith et al., 2003a, 2003b) topographic profiles (which are publicly available at the Planetary Data System database, www.pds-geosciences.wustl.edu). at the position of the graben's maximum width, so that graben topography is well captured by the altimeter, which records elevation data points every 300 m, approximately. Additionally, profiles are selected at the minimum angle possible relative to the orthogonal of the structure. This workflow ensures that the selected topography is representative of the structure. Then we projected each profile orthogonally to the graben, normalized the elevations relative to the shallowest point of each profile, and the distances relative to the deepest point of the trough (Fig. 1e). Each structure shows a distinct geometry which resembles differently the ideal geometry of a recent dike-induced graben as known from terrestrial examples (i.e. steep to subvertical walls, a sharp break in slope at the base and a flat floor). Galaxias Fossae is a narrow (<1.6 km) and shallow (<100 m) graben with gentle walls and a wide and flat floor (Fig. 1b and e). Moreover, the Galaxias Fossae graben widens toward the NW giving way

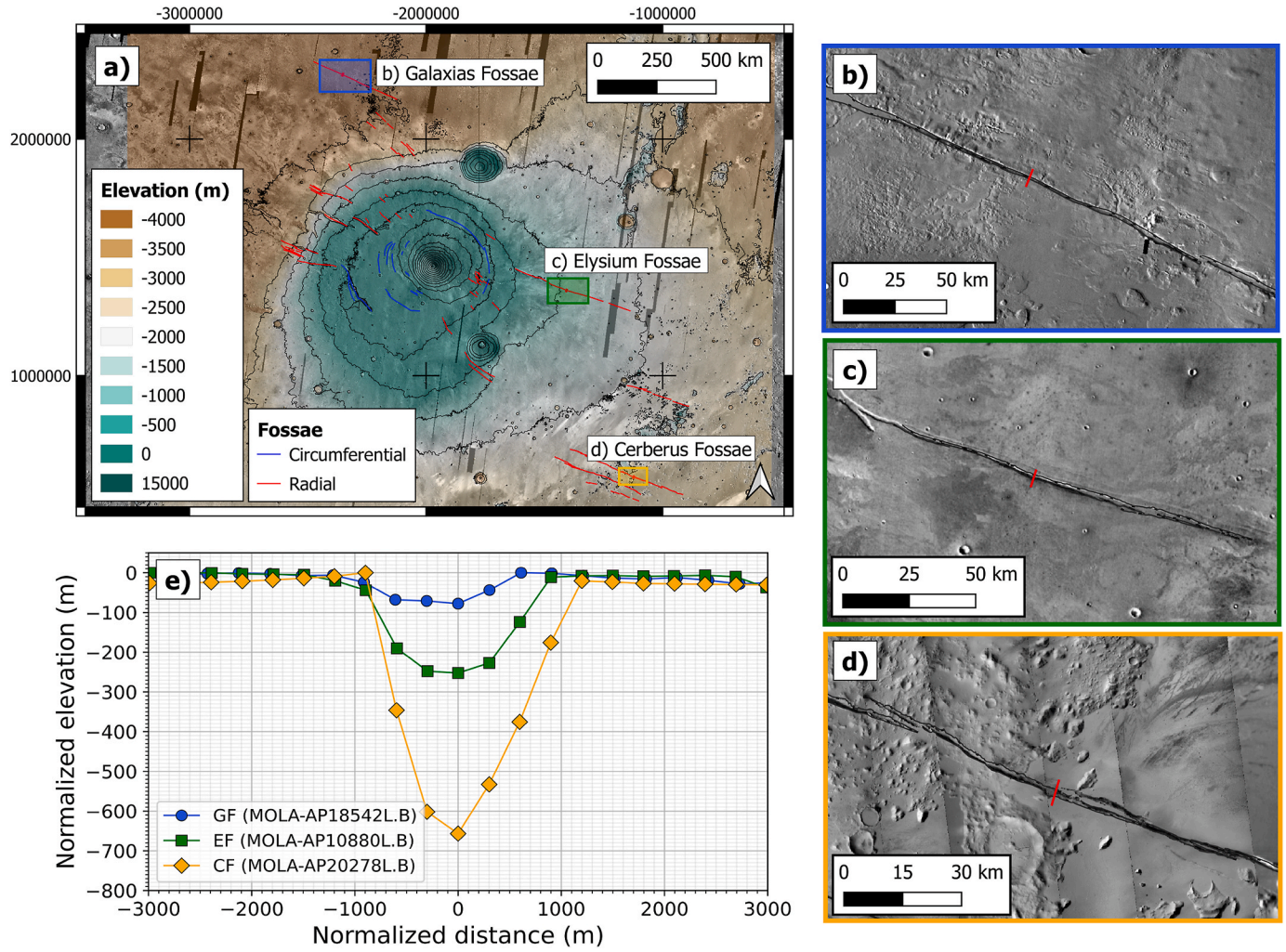

Fig. 1. a) Context map of the selected areas of study in the Elysium Bulge. Contour spacing is 1000 m and the deepest contour is −4000 m. Radial and circumferential fossae systems are indicated, many of which are likely associated to dikes at depth. b) Galaxias Fossae (GF). c) Elysium Fossae (EF). d) Cerberus Fossae (CF). The solid red line indicates the location of the chosen cross section in each case. e) Topographic profiles for all three sites. In parenthesis, the corresponding PEDR track. Note that these have been normalized in the vertical relative to the highest elevation found along the length of the cross section, and in the horizontal relative to the deepest point of each graben. (For interpretation of the references to color in this figure legend, the reader is referred to the Web version of this article.)

to an even wider segment with a smooth flat floor and eroded scarps. As previously discussed, NW Elysium is dominated by Late Hesperian and Amazonian units in which fluvial sediments from outflows and periglacial processes are common (Tanaka et al., 2014; Gallagher et al., 2018). Therefore, Galaxias Fossae, although young, may be the most affected by geomorphological agents, and the least fresh of all three cross sections. Elysium Fossae is wider (1.8 km), deeper (240 m) and shows a U-shaped profile, with smoother graben walls and a narrower but still flat floor (Fig. 1c and e). Some scarp erosion can be observed in the NW edge of the system toward Elysium Mons (Fig. 1c), but this is mostly absent from the rest of its length. Therefore, graben topography should be expected to be relatively fresh. The Cerberus Fossae graben is by far the largest structure, at 2.1 km width and up to 700 m depth (Fig. 1d and e). It shows steep graben walls, a narrow, possibly flat floor, a characteristic V-shape geometry, and most fault scarps are rough with no smoothing present. These features support the absence of erosion and thus the previously discussed young age of the system, which implies that the CF graben morphology is relatively fresh.

2.2. Cross section area balancing

Under the assumption that the observed graben are dike-induced and bound by a pair of normal faults, we used the lost graben area relative to their pre-deformational state to calculate the depth of the base of the layer in which extension is accommodated by normal faulting, hypothesized here to be the depth of the upper dike tip (D_d). A fully detailed description of this methodology and its associated uncertainties can be found in Rivas-Dorado et al. (2021), but we provide here a summary for reference. For a given graben topography, the input parameters required for this calculation are, in the coordinate system of the section: 1) the position of both fault scarps, 2) graben depth, 3) dip angle for the graben-bounding faults, and 4) two points at the edges of the cross section which define a line used to approximate the pre-deformational topography, or regional level (see Fig. 3a in Rivas-Dorado et al., 2022). With these, the graben area (A_g) is calculated as the area of the polygon defined between four points: the intersection of the regional line with each fault trace, and the intersection of each fault trace with a horizontal line at the given graben depth. Then, the sum of the horizontal distances between the top of the fault scarp and the intersection of the fault trace with the graben floor line provides the cumulative horizontal displacement (d) (i.e. the sum of the heave of both graben bounding faults). A_g and d allow to calculate the dike tip depth (D_d) through the concept of area preservation, i.e., that the area lost by the graben is equal to the area displaced laterally from the regional level to

the root of the structure (Chamberlin and Salisbury, 1909; Chamberlin, 1910)

$$D_d = \frac{A_g}{d} \quad (1)$$

Assuming that graben extension is entirely due to the accommodation of dike opening, the cumulative heave d is used as a proxy for dike aperture (a) (see Fig. 3b in Rivas-Dorado et al., 2022). Additionally, we estimate dike half-height (b) as the difference between dike tip depth measured relative to the graben floor and the depth of the planetary Level of Neutral Buoyancy (LNB = 10 km, Scott, 2002). This is done to obtain a full 2D dike geometry, which is required in later modeling stages, and is a plausible assumption, since previous numerical models and calculations have shown that dikes on Mars may extend vertically over distances comparable to twice the depth of the LNB (Rivas-Dorado et al., 2021, 2022).

2.3. Model of the fracture-induced stress field

We obtain the compound stress field around a dike opening in the subsurface in a 2D elastic space by using the dike geometry parameters obtained from area balance, the canonical model of fracture opening (Pollard and Segall, 1987; Pollard and Martel, 2020) and the stress field caused by the lithostatic load. For the fracture-induced stress field we use a rock mechanics tension-positive convention, in which tensional stresses are positive and compressional stresses are negative (Schultz, 2019, Chapter 3). Therefore, the driving stress acting on the crack walls in a direction orthogonal and opposite to these is positive, whilst all lithostatic stresses working against fracture opening are negative (Fig. 2). The dike is idealized as a surface in the (X, Y) plane with its aperture or width along (X) and its height or vertical extent along (Y) (Fig. 2). Dike length extends infinitely into and out of the page along (Z) and its geometry is assumed to be unmodified in this direction. Therefore, plain strain conditions (i.e., a *thick plate* approximation) are assumed, under which the 2D equations for displacement and stress derived from Cauchy's laws of motion are valid (Muskhelishvili, 1953; Pollard and Segall, 1987; Pollard and Martel, 2020). The use of these equations also implies the modeling of a homogenous, isotropic, and isothermal medium, in which the conditions required for linear elasticity are valid. The vertical axis of the dike is placed approximately at X = 0, and the entirety of the dike is at Y < 0. The position of the upper and lower tips of the dike are defined from the results of area balancing as D_d and D_d+2b, respectively (Fig. 2). The surface is at Y = 0, and all points at depth have values < 0. The dike is embedded in a single layer with homogeneous density, elastic (Young's Modulus E, and Poisson's ratio v) and frictional properties (tensile strength T, and coefficient of internal friction μ′).

The chosen boundary conditions are the tractions or stresses applied on the crack surface (Fig. 2). σ_I is the driving stress opening the dike along X, and σ_{II} is the driving shear stress parallel to the dike walls acting along Y. We calculate σ_I using the simple form of the plain-strain scaling between excess pressure and aperture (Pollard et al., 1983)

$$\sigma_I = \frac{a\mu}{2b(1-\nu)}, \quad (2)$$

where a is dike aperture in m, b is dike half-height in m, ν is Poisson's ratio, and μ is shear modulus or rigidity, in Pa. Therefore, this represents the final dike driving stress for the estimated aperture. Because we only model opening-mode fractures, $\sigma_{II} = 0$ in all cases.

The displacements and stresses around the crack are then calculated for every point in the grid using a tri-polar coordinate system. This uses two parameters, R and Θ, determined by the position of each point relative to the dike's upper and lower tip, and its center

$$R = (r_1 + r_2)^{0.5} \quad (3)$$

$$\Theta = \frac{\theta_1 + \theta_2}{2} \quad (4)$$

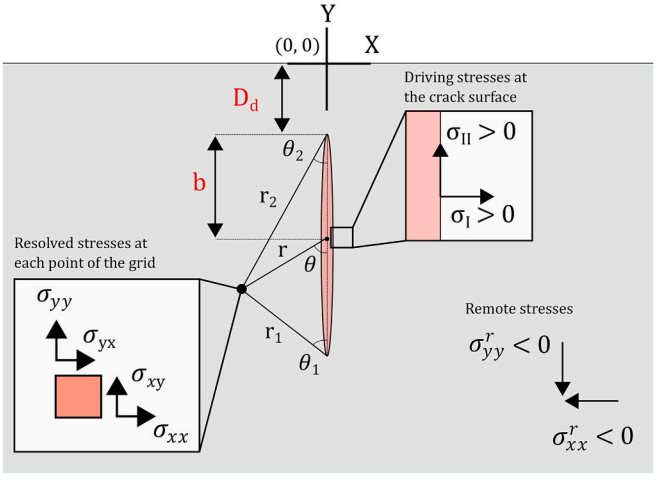

Fig. 2. Setup, coordinate reference system, input, and output parameters of the dike models. The driving stresses applied on the dike walls (σ_I, σ_{II}), and the remote stresses induced by the lithostatic load (σ^r_{xx},σ^r_{yy}) are used to calculate the resulting stresses at each point (σ_{xx}, σ_{yy}, σ_{xy}), represented by the square in the inset to the left. The parameters in red are those directly derived from the area balance methodology, which are used to define dike geometry. (For interpretation of the references to color in this figure legend, the reader is referred to the Web version of this article.)

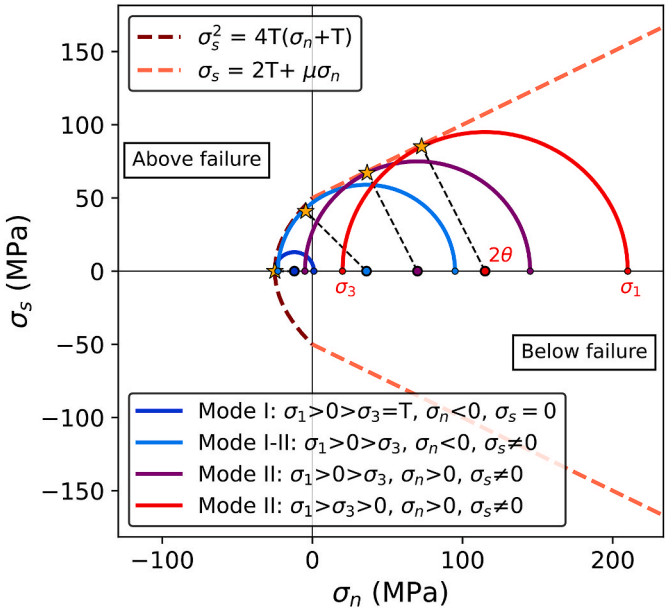

Fig. 3. Modified Griffith criterion used to determine if a point is below, at, or above failure, and the four possible modes of yielding for four combinations of principal stresses. The values of the principal stresses (σ_1,σ_3) are plotted in the σ_n axis (indicated in the red circle), which results in a circle which may or may not touch the failure criterion. In the examples, the yellow stars indicate the contact point between the circles and the criterion and mark the values of normal (σ_n) and shear (σ_s) stress under which failure occurs. The 2θ angle is the angle between σ_1 in the horizontal and the line between the circle center and the failure point, and indicates the angle of the normal to the failure plane relative to σ_1. The failure criteria is drawn with T = −25 MPa and $\mu' = 0.57$, and both the negative and positive realms of the shear stress are plotted. (For interpretation of the references to color in this figure legend, the reader is referred to the Web version of this article.)

then, the in-plane fracture-induced stresses are calculated (Pollard and Segall, 1987),

$$\sigma_{xx} = \sigma^r_{xx} + \sigma_I \left[rR^{-1}\ cos(\theta - \Theta) - 1 + b^2 rR^{-3}\ sin\ \theta\ sin\ 3\ \Theta \right] + \sigma_{II} \left[b^2 rR^{-1}\ sin\ \theta\ cos\ 3\ \Theta \right] \quad (5)$$

$$\sigma_{xy} = \sigma^r_{xy} + \sigma_{II} \left[rR^{-1}\ cos(\theta - \Theta) - 1 - b^2 rR^{-3}\ sin\ \theta\ sin\ 3\ \Theta \right] + \sigma_I \left[b^2 rR^{-1}\ sin\ \theta\ cos\ 3\ \Theta \right] \quad (6)$$

$$\sigma_{yy} = \sigma^r_{yy} + \sigma_I \left[rR^{-1}\ cos(\theta - \Theta) - 1 - b^2 rR^{-3}\ sin\ \theta\ sin\ 3\ \Theta \right] + \sigma_{II} \left[2rR^{-1}\ sin(\theta - \Theta) - b^2 rR^{-3}\ sin\ \theta\ cos\ 3\ \Theta \right] \quad (7)$$

where σ^r_{xx} is the remote stress acting against dike opening along (X), σ^r_{xy} is the remote shear stress, σ^r_{yy} is the lithostatic vertical stress on (Y), σ_{xx} is the resulting in-plane stress along (X), σ_{yy} is the resulting stress in (Y), and σ_{xy} the shear stress. A square element may be imagined at each point of the grid for which the final stresses are calculated, where σ_{xx} is the stress that acts normal to the face of the element facing the X axis, σ_{yy} operates normal to the face of the element facing Y, and σ_{xy} orthogonal to each of these stresses (Fig. 2). The remote stresses, σ^r_{xx} and σ^r_{yy}, are calculated at each point as function of the lithostatic stress, where the normal vertical stress is

$$\sigma^r_{yy} = \rho g Y \quad (8)$$

where ρ is an average basalt density of 2900 kg m^{-3} in all models, g is the Martian gravitational acceleration of 3.7 m s^{-2}, and Y is the depth at each point of the grid. Negative depths ensure that lithostatic stresses are negative as per the convention used. The normal horizontal and shear stresses are calculated from the normal vertical stress for a compressible medium

$$\sigma^r_{xx} = \sigma^r_{yy} \left(\frac{\nu}{1 - \nu} \right) \quad (9)$$

where v is Poisson's ratio. Equations (8) and (9) are substituted in equations (5)–(7), to obtain the total stress field around the opening dike. The equations are valid for quasi-static conditions and thus require preservation of angular momentum, which implies that $\sigma^r_{xy} = \sigma^r_{yx} = 0$. These sets of equations allow to obtain the full instantaneous state of stress around an opening fracture embedded in a linearly elastic medium under plane-strain conditions.

2.4. Application of the failure criterion

We use the resulting stress field to calculate the magnitude and orientations of the principal stresses around the dike, and the modified Griffith criterion to define the locations at which failure occurs and under which mode. Firstly, we switch to a compression-positive convention and compute the principal stresses, σ_1 and σ_3, from the final stress field. We do this because faulting and fracturing problems in structural geology are most frequently solved in this convention, in which $\sigma_1 > \sigma_3$, and where $\sigma_i > 0$ indicates compression, in contrast to the rock mechanics tension-positive convention. Thus, we change the signs of σ_{xx}, σ_{yy} and σ_{xy}, and obtain the principal stresses at each point of the grid through (Jaeger et al., 2007)

$$\sigma_{1,3} = \left(\frac{\sigma_{xx} + \sigma_{yy}}{2} \right) \pm \sqrt{\left(\frac{\sigma_{xx} - \sigma_{yy}}{2} \right)^2 + \sigma^2_{xy}} \quad (10)$$

where the positive sign corresponds to σ_1, and the negative sign to σ_3. Additionally, the clockwise orientation of σ_1 relative to the X axis, ψ, is given by (Jaeger et al., 2007):

$$2\psi = tan^{-1} \frac{2\sigma_{xy}}{\sigma_{xx} - \sigma_{yy}} \quad (11)$$

This allows to plot the orientations of both principal stresses and later the orientation of the failure planes with respect to the principal stresses. Supplementary Fig. 1 shows the final dike-induced stresses, principal stresses, and principal stresses orientation (dike only and dike + lithostatic stresses) for a set of example input parameters.

Once the principal stresses are calculated, the modified Griffith criterion allows to determine if each point is below, at, or beyond failure (Fig. 3). The modified Griffith criterion is used since it allows to express failure in terms of tensile strength, T, which can be related analytically to compressive strength, C, and thus allows to properly account for tensile failure when evaluating the stress state. The modified Griffith criterion is applied using (Schultz, 2019)

$$\text{For } \sigma_n < 0 : \sigma^2_S = 4T(\sigma_n + T) \quad (12a)$$

$$\text{For } \sigma_n > 0 : \sigma_s = 2T + \mu' \sigma_n \quad (12b)$$

where σ_s is shear stress, σ_n is normal stress, T is tensile strength, μ' is the coefficient of internal friction, and θ is the angle from σ_1 to the outer normal of the failure plane (Fig. 3). Note in 12b that C = 2T, with C being cohesion. This follows from solving for $\sigma_n = 0$ in 12a, which yields the value of the inherent shear strength under which failure occurs if the normal stress is zero. However, experimental values of the uniaxial tensile strength and cohesion suggest that the latter is frequently much larger than tensile strength (Bieniawski, 1984).

When a combination of principal stresses results in a circle which is tangent to the failure criterion, the point is at failure and the values of σ_n, σ_s, and 2θ, are calculated. This may occur under four modes in the models, depending on the combination of the principal stresses and the stresses at the discontinuity (Fig. 3):

1. When $\sigma_1 > 0 > \sigma_3 = T$, no other point in the Mohr circle is at or above equation (12a) failure criterion, and therefore $\sigma_n < 0$ and $\sigma_s = 0$ (Fig. 3, blue circle). Tensile failure occurs through mode I cracks, or joints, in which the walls of the discontinuity separate from one another orthogonally to their strike without shearing (first mode). 2θ is 180°, which implies that the failure plane is parallel to the principal compressive stress.
2. When $\sigma_1 > 0 > \sigma_3$, tensile-compressional failure may occur when the Mohr circle is tangent to either equation (12a) or 12b. In both cases, the shear stress is non-zero, but the outward normal stress may be negative or positive.
   a. If the circle is tangent to equation (12a), then $\sigma_n < 0$ and $\sigma_s \neq 0$ (Fig. 3, light blue circle), which implies the formation of mixed mode I-II discontinuities in which their walls separate from one another both orthogonally and parallel to the failure plane (second mode).
   b. Oppositely, if the circle is tangent to equation (12b), then $\sigma_n > 0$ and $\sigma_s \neq 0$ (Fig. 3, purple circle), which implies the formation of mode II discontinuities, i.e., faults, where the walls are compressed against each other and sheared along the failure plane (third mode).
3. Finally, if $\sigma_1 > \sigma_3 > 0$, failure occurs under general compression when the circle is tangent to equation (12b), and therefore $\sigma_n > 0$ and $\sigma_s \neq 0$ (Fig. 3, red circle). Because the shear stress is non-zero and the normal stress is positive, this implies the formation of mode II faults (fourth mode).

The θ angle provides the orientation of the normal of the fracture plane relative to σ_1. For a point that is found at failure there will always be two conjugate planes owing to the symmetry of the stress functions. In our models we plot only one of the conjugate planes, that with an orientation favorable to the normal faults inferred from the surface topography. For joints or mode-I cracks, and because these are parallel to σ_1, there is only one possible orientation, which is plotted.

The workflow described so far allows to determine if the points in the

medium surrounding a dike with a given geometry and driving stress will be below, at, or beyond failure.

2.5. Modeling methodology

We varied key input parameters to create a sufficiently large number of scenarios at each location (Table 1) and ran a dynamic model in each to gain insight in the early processes that take place during diking.

The most relevant input parameters are fault dip (β), friction coefficient (μ′), Young's Modulus (E) and tensile strength (T). Smaller fault dips result in wider and shallower dikes, and vice versa. In turn, dike aperture determines final driving stress pressure (equation (1)), and the depth of the upper dike tip will condition the interactions of the dike-induced with the lithostatic depth-dependent stresses. A ±10% change in fault dip can result in changes of ≈ ±30% of dike depth and apertures (Rivas-Dorado et al., 2021) and therefore we use three fault dips: 55°, 60° and 65°, covering a range of plausible dip angles for normal faults (e.g., Chadwick and Lucchitta, 1993; Schultz and Lin, 2001; Vaz et al., 2014). Because μ′ determines fault dip at depth and is lithology-independent (Scholz, 2002), we use a single coefficient of internal friction per fault dip modeled. The relationship between the two is given by:

$$\mu' = tan\ (2\beta - 90) \tag{13}$$

Where, β is the fault dip. This expression can be derived from the trigonometric relationships between the angle of internal friction, 2θ, and its complementary angle α (the angle between σ_1 and the plane of the discontinuity) in the Mohr circle. Therefore, we use friction coefficients of 0.36, 0.58, and 0.84, for the values of fault dip 55°, 60° and 65°, respectively.

The host rock mechanical properties determine both the dike driving stresses and the rock's response to stress. Three sets of mechanical properties representing a range of low, intermediate, and high compliance host rocks were selected for each fault dip used. Firstly, location-specific values of increasingly large Young's Modulus were chosen so that the average final driving stresses modeled at each site do not greatly exceed 60 MPa (Table 1). This is a plausible maximum tensile strength for intact basalts (Lama and Vutukuri, 1978; Bieniawski, 1984; Schultz, 1995; Apuani et al., 2005), and thus, for realistic maximum driving stresses. This is done because driving stress is dependent both on E and aperture (see equation (1)), and very different apertures are obtained in each case. For example, the Cerberus Fossae dikes are inferred to be up to several hundred meters thick. In this case, using the elastic properties of a highly compliant rock would lead to unrealistic driving stresses of hundreds of MPa. Thus, mechanical properties of a relatively weaker host must be used to obtain reasonable driving stresses in this case (Rivas-Dorado et al., 2022). Secondly, three increasingly large values of T (2, 4 and 6 MPa) were used to represent weakened or porous to moderately competent materials in volcanic edifices (Schultz, 1995; Thomas et al., 2004; Apuani et al., 2005; Heap et al., 2021). Therefore and in summary, for each location three fault dips were used to model the dikes, and for each of these scenarios three sets of properties to represent a weak, medium, and strong host rock were tested, resulting in 27 model combinations, 9 at each site, which are shown in Table 1.

For each model we calculate the stress evolution (thus, they are dynamic models) of the elastic medium surrounding the intrusion as driving stress increases in $n = 100$ timesteps from 0.5% to an appropriate percentage of the final excess pressure. The initial range chosen for all models was 0.5–20%, which was later adjusted to an appropriate range in each model. At each model step the full stress state is calculated and evaluated to determine if failure occurs at any point in the grid. When a point at a given timestep is found at failure, the values of normal and shear stress, and the orientation of the failure plane, are stored for the following timesteps. In other words, the algorithm records at each point the values and plane orientation when failure is first found. A sufficiently large number of timesteps ensures that if a point may reach failure with a given stress path this will be captured. The final timestep shows the points where failure was found and the orientation of the

Table 1
Key input and output parameters, identifiers, and file names of all the models constructed.

Location	W_g (m)	β	D_d (m)	a (m)	2b (m)	μ'	E (GPa)	μ (GPa)	T (MPa)	σ_I (MPa)	σ_I range (% σ_I)	1st near-surface tensile cracks (% σ_I)	Linkage (% σ_I)	a_i (m)	σ_i (MPa)	T-D (/D_d)	Model type	ID	File name
Galaxias Fossae	1500	55	-1082	88	17834	0.36	20	8	2	26	0-3.4	2.9	3.4	3.0	1.8	0.6	1	GF1	GF_sn_55_0.36_20.0_2.0.mov
							40	16	4	53	0-2.7	2.5	2.7	2.4	2.8	0.9		GF2	GF_sn_55_0.36_40.0_4.0.mov
							60	24	6	79	0-2.4	-			3.8	1.0		GF3	GF_sn_55_0.36_60.0_6.0.mov
		60	-1319	72	17360	0.58	30	12	2	33	0-5.2	4.0	5.1	3.7	2.3	0.6	1	GF4	GF_sn_60_0.58_20.0_2.0.mov
							40	16	4	44	0-3.9	3.6	3.9	2.8	3.5	0.7	2	GF5	GF_sn_60_0.58_40.0_4.0.mov
							60	24	6	66	0-3.6	3.5	3.6	2.6	4.8	1.0		GF6	GF_sn_60_0.58_60.0_6.0.mov
		65	-1641	58	16716	0.84	20	8	2	19	0-8.2	5.9	8.2	4.8	3.1	0.5		GF7	GF_sn_65_0.84_20.0_2.0.mov
							40	16	4	37	0-6.0	5.2	6.0	3.5	4.5	0.7	2	GF8	GF_sn_65_0.84_40.0_4.0.mov
							60	24	6	56	0-5.4	5.2	5.4	3.2	6.0	0.9		GF9	GF_sn_65_0.84_60.0_6.0.mov
Elysium Fossae	1900	55	-1308	336	17384	0.36	7.5	3	2	39	0-2.9	2.3	2.9	9.8	2.2	0.6	1	EF1	EF_sn_55_0.36_7.5_2.0.mov
							12	4.8	4	62	0-2.8	2.5	2.8	9.3	3.5	1.0		EF2	EF_sn_55_0.36_12_4.0.mov
							15	6	6	77	0-3.0	-	-		4.6	1.0		EF3	EF_sn_55_0.36_15_6.0.mov
		60	-1611	277	16776	0.58	7.5	3	2	33	0-4.5	3.2	4.5	12.5	3.0	0.5	1	EF4	EF_sn_60_0.58_7.5_2.0.mov
							12	4.8	4	53	0-4.1	3.6	4.1	11.4	4.3	0.9	2	EF5	EF_sn_60_0.58_12_4.0.mov
							15	6	6	66	0-4.5	4.3	4.5	12.5	6.0	0.9		EF6	EF_sn_60_0.58_15_6.0.mov
		65	-2024	223	15951	0.84	7.5	3	2	28	0-7.4	4.8	7.3	16.6	4.2	0.4		EF7	EF_sn_65_0.84_7.5_2.0.mov
							12	4.8	4	45	0-6.5	5.4	6.5	14.6	5.8	0.8	2	EF8	EF_sn_65_0.84_12_4.0.mov
							15	6	6	56	0-6.9	6.4	6.8	15.4	7.8	0.7	2	EF9	EF_sn_65_0.84_15_6.0.mov
Cerberus Fossae	2100	55	-1134	910	17731	0.36	5	2	2	68	0-1.4	1.2	1.4	12.7	1.9	0.6	1	CF1	CF_sn_55_0.36_5_2.0.mov
							7.5	3	4	103	0-1.45	1.4	1.5	13.2	3.0	0.9		CF2	CF_sn_55_0.36_7.5_4.0.mov
							10	4	6	137	0-1.55	1.5	1.5	14.1	4.2	1.0		CF3	CF_sn_55_0.36_10_6.0.mov
		60	-1444	750	17710	0.58	5	2	2	56	0-2.25	1.7	2.2	16.9	2.6	0.6	1	CF4	CF_sn_60_0.58_5_2.0.mov
							7.5	3	4	85	0-2.20	2.0	2.2	16.5	3.9	1.0	2	CF5	CF_sn_60_0.58_7.5_4.0.mov
							10	4	6	113	0-2.23	2.2	-	16.7	5.2	1.0		CF6	CF_sn_60_0.58_10_6.0.mov
		65	-1866	606	16267	0.84	5	2	2	50	0-3.75	2.5	3.8	22.7	3.7	0.5		CF7	CF_sn_65_0.84_5_2.0.mov
							7.5	3	4	75	0-3.55	3.0	3.6	21.5	5.3	0.9	2	CF8	CF_sn_65_0.84_7.5_4.0.mov
							10	4	6	99	0-3.55	3.3	3.6	21.5	7.1	1.0	2	CF9	CF_sn_65_0.84_10_6.0.mov
Generic example under Martian conditions			-1330	72	17834		50		1	17340	0-1.8	1.31	1.79	1.29	1.98	0.45		M	Mars_sn_60_50.0_0.78_1.5.mov
Generic example under terrestrial conditions			-1330	72	17834		50		1	17340	0-2.4	1.43	2.4	1.72	2.64	0.19		E	Earth_sn_60_50.0_0.78_1.5.mov

W_g: graben width, β: fault dip. D_d: top dike depth. a: dike aperture. 2b: dike height. μ': coefficient of internal friction. E: Young's Modulus. μ: shear modulus or rigidity. T: tensile strength. σ_I: driving stress corresponding to the total dike aperture. σ_i range: range of driving stresses modeled. 1st near-surface tensile cracks: % of σ_I at which the first joints appear at the surface. Linkage: % of σ_I at which linkage between the near-surface and at-depth discontinuity systems connect. a_i: dike aperture at the end of the range modeled. σ_i: dike driving stress at the end of the range modeled. T-D: extent of the Tension-Dominated section, as a fraction of D_d.. Compatible models in a weak, intermediate, and strong host rock are highlighted in light, bright and dark grey tones, respectively.

failure planes in each node. Fig. 4 shows an example of this where all possible modes of failure, as described in Section 2.4, are illustrated. In the models, the topography, and the faults based on the results of area balance are drawn for comparison with model outputs but bear no impact in the results.

The models presented here were ran through a *python* program, *DiES.py* which is publicly available (Rivas-Dorado, 2022). The program also allows to model the displacements (u_x, u_y and u_{xy}) and stresses (σ_{xx}, σ_{xy}, σ_{yy}, σ_τ) induced by an opening and/or shearing discontinuity which may be subject to driving stresses orthogonal (σ_I) and/or parallel (σ_{II}) to the crack surface. The code permits the creation of single or multi-layered models at the desired grid resolution, for which the mechanical and frictional properties of each layer are specified. Additionally, the effects of the lithostatic stresses can optionally be switched on and off to model the purely fracture-induced stresses, or the final stress field of an embedded discontinuity in the subsurface. It offers multiple options for performing the displacement and stress calculations only, plotting the different components of these, showing model properties, etc. Thus, it is a relatively simple but powerful tool, which can be applied to the investigation of problems related to opening-mode or shear discontinuities, and which we will continue to update in the future.

2.6. Model limitations

As discussed in Section 2.3, a key underlying assumption in our modeling is that the conditions of linear elasticity apply. This is true in the first steps of each model, until failure is first found. Therefore, in a strict sense, once a single discontinuity is formed the conditions for LEFM are no longer valid (i.e., the medium is not homogeneous or isotropic). Additionally, the newly formed discontinuities will move on to transfer part of the dike-induced stresses, thus changing the behavior of the system. In reality, the locus of discontinuity formation and fault nucleation depends on the pre-existing heterogeneities within the rock volume (Segall and Pollard, 1983; Willemse et al., 1997; Clifton and Schlische, 2001). Therefore, the location of cracks and faults as predicted in elastic models such as those presented in this work may not correspond with those that would form in true rock volumes. In any case, it is possible that during the early stages of diking the discontinuities remain disconnected, and therefore, that the medium maintained a near-elastic behavior. This is observed in the experiments by Mastin and Pollard (1988), in which the early stages see the development of isolated zones of failure (their Figures 13 a and b), which later coalesce into surfaces with dip slip (their Figure 13 c). Additionally, the deviatoric stress field induced by the dike may be dominant over the smaller stress fields associated to early fractures and faults, and thus, these may be

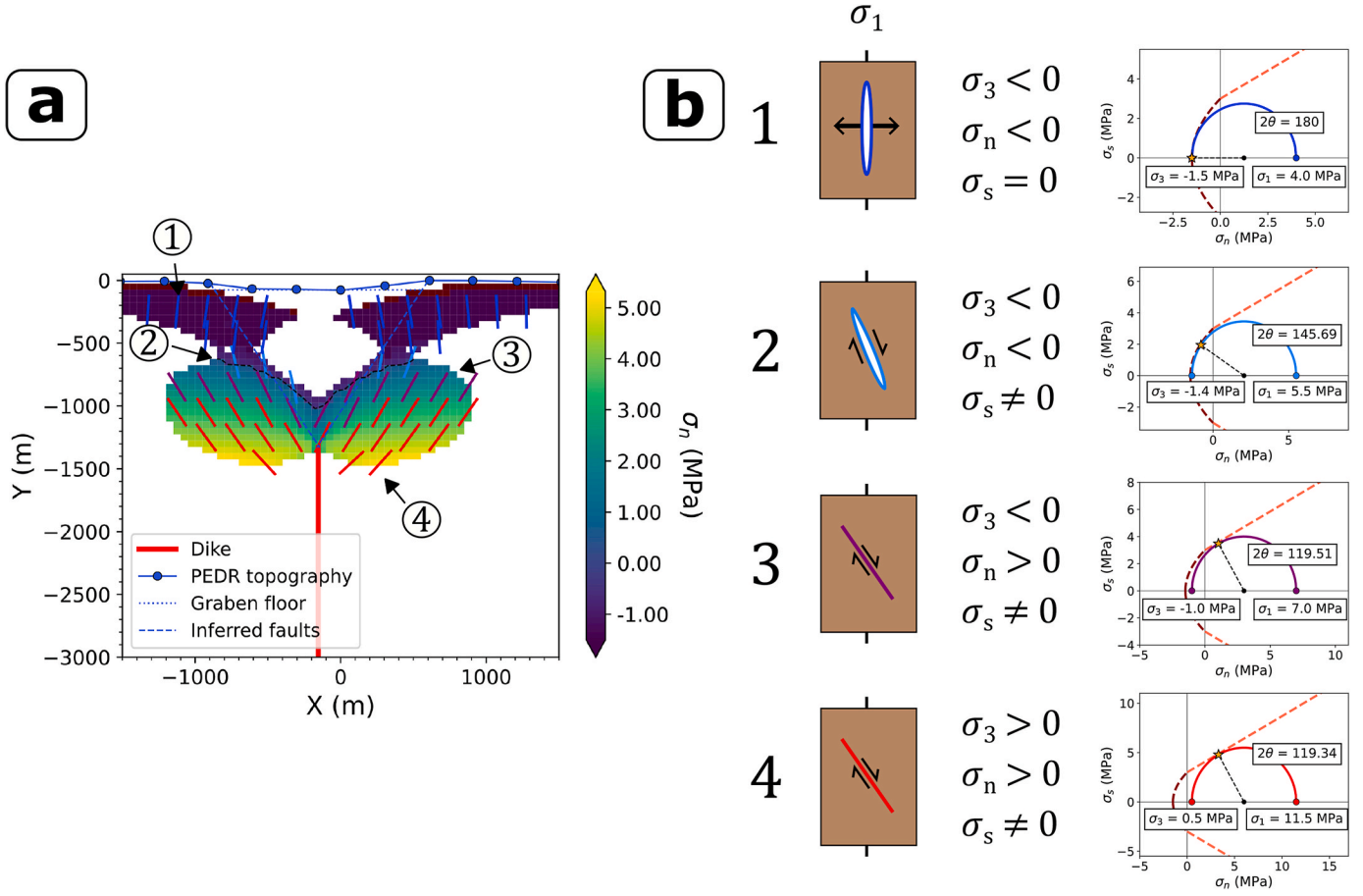

Fig. 4. a) Final result of a dynamic model using as input parameters the results of area balance on the GF cross section using a fault dip of 60°. This results in a dike with a = 72 m at D_d = 1330 m. With E = 30 GPa and v = 0.25, $\sigma_{I,final}$ = 33 MPa. The rest of the model parameters are: ρ = 2900 kg m^{-3}, T = −1.5 MPa, and μ' = 0.57. The model was run for driving stress between 0.5 and 3% $\sigma_{I,final}$ through 150 steps at a 50 × 50 m resolution. a_i and σ_i at the end of the model were 2.17 m and 2.0 MPa, respectively. The figure shows the values of normal stress at which failure is first found at each point, and a downsampled collection of the orientations of the failure planes (only those favorable to the formation of normal faults), overlying the normalized topography. The dashed contour indicates σ_n = 0. b) All possible modes of failure found in the models, illustrated by the example in 4a. To the left, a schematic representation of the discontinuity type. To the right, the approximate configuration of the Mohr circle for each type of discontinuity at the points indicated in 4a.

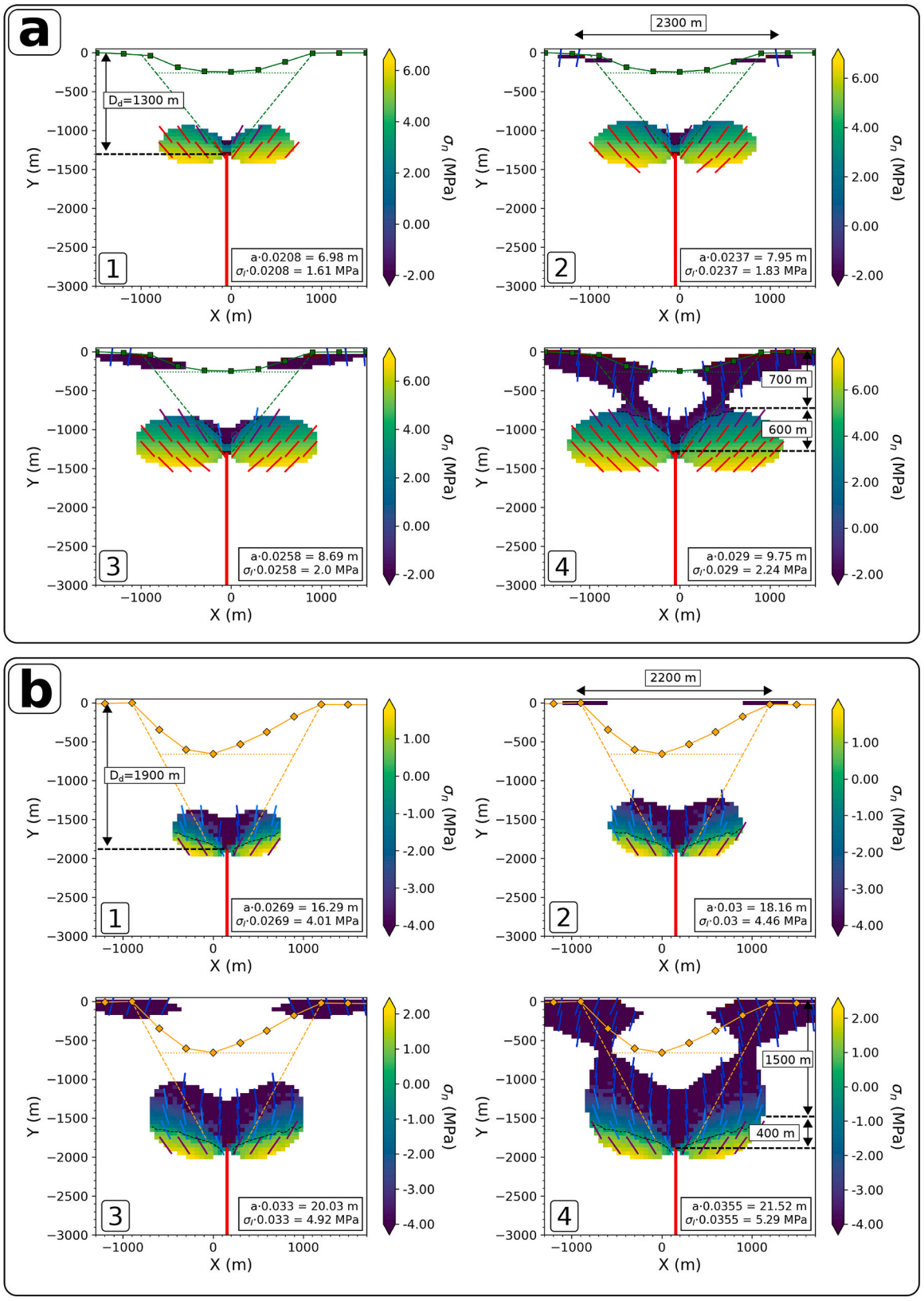

Fig. 5. Examples of dynamic models which are compatible with dike induced graben formation. The models are not shown at regular intervals but rather at key timesteps. a) Model EF1 as an example of a relatively shallow thick dike modeled through low dip faults, intruding a weak host rock. Fault dip: 55°, $\mu' = 0.57$, E = 20 GPa, $D_d = -1082$ m, a = 88 m, 2b = 17.8 km, $\sigma_I = 26$ MPa, T = 2 MPa. b) Model CF8 as an example of a relatively deep and thin dike modeled with higher fault dips, embedded in a relatively stronger host. Fault dip: 65°, $\mu' = 1$, E = 7.5 GPa, $D_d = -1895$ m, a = 606 m, 2b = 16.3 km, $\sigma_I = 75$ MPa, T = 4 MPa. The evolution of steps 1 to 4 are described in Section 3 for both numerical model examples.

considered negligible in these early stages. If this is the case, then our models may be a useful first approximation to understand what types of discontinuities may be formed during the early stages of diking. As the models evolve, it becomes more likely that discontinuities connect and therefore, that the conditions of elasticity are fully broken. Consequently, our models need to be restricted to relatively small percentages of the final driving stress, as described in Section 2.5, in which effective linkage between discontinuities is less likely to have taken place.

The elastic equations used here calculate stresses and displacements which are maximum at the dike center and minimum at its tips, and thus, implicitly describe a dike with an elliptical shape and a sharp termination. However, dike tip geometry (blunt versus elliptical) has been recently identified as a key factor in the failure style ahead of the dike tip (Trippanera et al., 2016; Walker et al., 2021), and thus, potentially in the structures developed between the latter and the surface during dike opening. The methodology presented in this work accounts only for stress distributions resulting from elliptical dikes but could potentially be adapted to model blunt-ended dikes and their corresponding stresses.

3. Results: models compatible with dike-induced graben nucleation

We qualitatively define as 'compatible' the models in which the mode of discontinuities formed, their sequence, and location, are consistent with the formation of the inferred present-day graben-bounding faults (e.g., Fig. 4a). Models compatible with normal fault nucleation above the dike were found in two general scenarios: 1) lower dip angle normal faults above shallow and narrow dikes in a relatively weak host rock, and 2) higher dip angle faults above deeper and wider dikes in a more compliant host. Table 1 shows that for the 55° dip fault models, only 3 compatible scenarios are found, all in models with relatively weak mechanical properties. For the 60° dip models, compatible scenarios are distributed so that 3 correspond to weak models and 3 to models with intermediate properties. For the 65° dip models, compatible scenarios are distributed so that 3 correspond to models with intermediate properties, and 2 to models with strong mechanical properties. Selected examples illustrative of the two general scenarios are shown in Fig. 5, but the animations and a specific discussion for each model can be found in the Supplementary Materials to this article.

For low dip faults, shallow dikes, and a weaker host, mode II discontinuities formed under general compression and tension-compression eventually link with tensile fractures nucleated at the surface location of the present-day faults (Fig. 5a). Models in which this behavior is observed are GF1, GF4, EF1, EF4, CF1, CF4 and CF7 and their evolution is very similar, with changes in the percentage relative to the final driving stress (% σ_I) at which the successive steps take place (Table 1), and in the exact location at which the first surface joints form. Fig. 5a illustrates this using EF1 as an example. The first features formed are mode II discontinuities (normal faults) under general compression which appear immediately above and to the sides of the dike tip, as early as 0–2% σ_I (Fig. 5a, Step 1). Normal faults in general compression are dominant above the dike tip and to the outer sides of the symmetric lobes, whilst faults in tension-compression are prevalent in the central portion. The first mode-I cracks form slightly below the model surface and close to the position of the present-day faults at 2.4% σ_I, as the faults propagate away from the dike tip (Fig. 5a, Step 2). As driving stress increases to 2.6% σ_I, the surface joints propagate toward the graben center and at depth. Simultaneously, a larger number of faults under tension-compression propagate upward in the central region (Fig. 5a, Step 3). Eventually, linkage between the shallow and deep discontinuity systems occurs at 2.9% σ_I, coupled with the formation of mixed-mode cracks in the transition zone between faults and tension cracks (Fig. 5a, Step 4). In the final timestep, tensile cracks occupy 53% of the vertical section from the surface to the dike tip, whilst 46% corresponds to normal faults formed either under general compression or tension-compression (Table 1). At this stage it is likely that the discontinuities formed are effectively linked, leading to non-elastic behavior. Thus, our models may not be appropriate after this point, although the dike may continue to grow in thickness, and the faults continue to accommodate stress.

For higher dip faults, deeper dikes, and a stronger host, tensile cracks formed at the surface at the location of the present-day faults may collapse at depth into normal faults and join with either mixed-mode or mode-II discontinuities formed under tension-compression propagated from the dike tip. The corresponding models are GF5, GF8, EF5, EF8, EF9, CF5, CF7, CF8 and CF9 (Table 1). Fig. 5b shows an example of this using CF8. The first discontinuities formed are mode-I cracks above the dike tip, and either mixed mode I-II or mode II discontinuities at its sides, at 2.7% σ_I (Fig. 5b, Step 1). These continue to grow toward shallower depths in two symmetric lobes as σ_I increases to 3% σ_I, when the earliest near-surface mode-I cracks form at the location of the present-day faults (Fig. 5b, Step 2, near-surface purple cells). The model is then dominated by joints which grow both from the surface to depth and vice versa, at the top of the propagating lobes. This is coupled with the development of mixed-mode cracks in the central part of the lobes, and faults formed under tension-compression at the base (Fig. 5b, Step 3). Finally, linkage between the shallow and deep joints occurs at 3.5% σ_I (Fig. 5b, Step 4). In the final timestep, the tension-dominated region extends from the surface to approximately 78%·of the distance to the dike tip, and the remainder 22% is dominated by mixed-mode discontinuities (Table 1). As in the previous case, because effective linkage between the discontinuities formed may take place after this step, our models should not be extended beyond this point.

The rest of the models do not show compatible configurations with normal fault nucleation. For example, models of relatively shallow dikes (i.e., low dip faults) in stiffer rocks tend to produce significant tensile fracturing which propagates quickly from the dike tip to the surface (models GF3, GF6, GF9, EF3, EF6, CF3 and CF6). If effective linkage between these fractures occurs these scenarios are likely to evolve into eruptions, which will preclude further graben growth and dike widening. Since these models produce few to no discontinuities with dip-slip in the vicinity of the dike tip, we take them as less likely to appropriately nucleate full normal faults. Models of deep dikes (i.e., high dip faults) in low-compliance rocks are generally classified as incompatible with the observed graben (models GF7, EF7, CF7). This is because the breadth of the tensional stresses at surface is such that failure occurs at a distance away from the location of the present-day faults, and thus any joints which at depth may collapse into dip-slip surfaces and aid in the nucleation of normal faults do not match that of the current fault scarps. This is also true for the symmetric lobes where faults are predicted, which also propagate away from the faults. These conditions would favor the formation of wider graben than observed, and support their classification as non compatible.

4. Discussion

4.1. Interpretation of the modeled physical processes

Any dike intruding the subsurface of a planetary lithosphere will do so acting against the established stress field in which, provided that additional tectonic forces are absent, the maximum compressive stress will be vertical. On the other hand, the compressive stresses induced by the dike are orthogonal relative to the dike walls at its center and rotate to become subvertical (even outward dipping) above the dike tip (see Supplementary Figs. 1a and b). Therefore, both the lithostatic and dike-induced stresses work in favor of a vertical maximum principal stress above the dike and close to the surface. Even with a relatively small dike-induced stress, this is the cause of the ubiquitous presence of near-surface subvertical fissures and tensile cracks. These are observed in many recent diking episodes (Pollard et al., 1983; Kuntz et al., 2002;

Yirgu et al., 2006; Pallister et al., 2010; Jónsson, 2012; Trippanera et al., 2019), and most dike intrusion laboratory experiments have reproduced them in the early stages of diking (Mastin and Pollard, 1988; Trippanera et al., 2014, 2016; Poppe et al., 2019).

At depth, faulting and jointing are a product of the complex interaction between the principal stresses, which depend on the dike and lithostatic stresses, and the failure criterion. The dike and lithostatic stresses depend on dike geometry, dike depth, host rock density and elastic properties, whilst the failure criterion depends on the host rock frictional properties. Firstly, for low compliance rocks a given dike aperture requires a smaller driving stress than for a competent rock, as per equation (2). Additionally, dikes at lower depths resulting from assuming lower dip faults have greater apertures, and vice versa for dikes at greater depths. Thus, in our models, the larger final driving stresses correspond to shallow dikes in stronger host rocks, and smaller values are found for deep dikes in less competent hosts. On top of this, in dikes emplaced at shallow depths the magnitude of the compression exerted by the lithostatic stress is smaller than that for dikes emplaced at greater depths, as per equations (7) and (8). In other words, dike-induced stresses are dominant in shallower relative to deep dikes. By considering the interaction between these factors, we can generally interpret the models.

Near the dike tip, a host rock with low-compliance elastic properties and a low tensile-compressive strength is more likely to fail under general compression ($\sigma_1 > \sigma_3 > 0$) rather than under tension-compression ($\sigma_1 > 0 > \sigma_3$) or tension ($\sigma_1 > \sigma_3 = T$), for a given dike aperture. This is because as T becomes lower (less negative), the failure criterion is pushed toward the compressive realm, and thus if failure is found this will more likely occur at ($\sigma_1 > \sigma_3 > 0$), and therefore at ($\sigma_n > 0$, $\sigma_s \neq 0$). In other words, the failure modes shown in Fig. 4b3 and 4b4 become more common, as shown by the relatively larger extent of the compression-dominated versus the tension-dominated vertical section in the low strength models (e.g., models GF4 vs GF5, EF4 vs EF5, or CF4 vs CF5). This is especially true in deep dikes, where the lithostatic compressive stresses work in favor of maintaining a compressive regime through most of the section, and structures under general compression are significantly more dominant (e.g., GF7, EF7, or CF7). In these cases, however, the amplitude of the stresses at surface leads to the formation of tensile cracks located far from the present-day location of the faults, leading, as discussed previously, to incompatible models. The processes in shallow dikes are similar, but the dike stresses have a greater weight due to the relatively smaller lithostatic stresses. Interestingly, because of the larger final σ_I which corresponds to shallower dikes, a smaller % of this value is needed to achieve the end point of the models, resulting in the compatible models requiring smaller σ_I than in deeper dikes (1.78–2.24 MPa for models with $\beta = 55°$, versus 3.05–4.15 MPa, for models with $\beta = 65°$). Opposite to the previous case, the narrower breadth of the surface tensional stresses for shallow dikes leads to compatible models (e.g., GF1, GF4, EF1, EF4, CF1, CF4). In summary, a small aperture and a shallow dike are required in a low-compliance host to produce a failure sequence which favors graben nucleation through a mixture of mode I and II discontinuities.

Oppositely, a host rock with high-compliance elastic properties and a high tensile-compressive strength is more likely to fail under tension-compression ($\sigma_1 > 0 > \sigma_3$) or tension ($\sigma_1 > \sigma_3 = T$) close to the dike tip, for a given dike aperture. This is because the failure criterion is pushed toward the tension realm, which allows the rock to sustain the increase of a larger dike-induced tension until ($\sigma_3 = T$). Equivalently, the failure modes shown in Fig. 4b1 and 4b2 become more common. This effect is more intense in shallower dikes and causes the quick formation of swarms of tensile cracks from the tip to the surface and vice versa, which leads to incompatible models, as previously discussed. This can be quantified by the small difference between the % σ_I at which the first tension cracks form at surface, and that at which the linkage

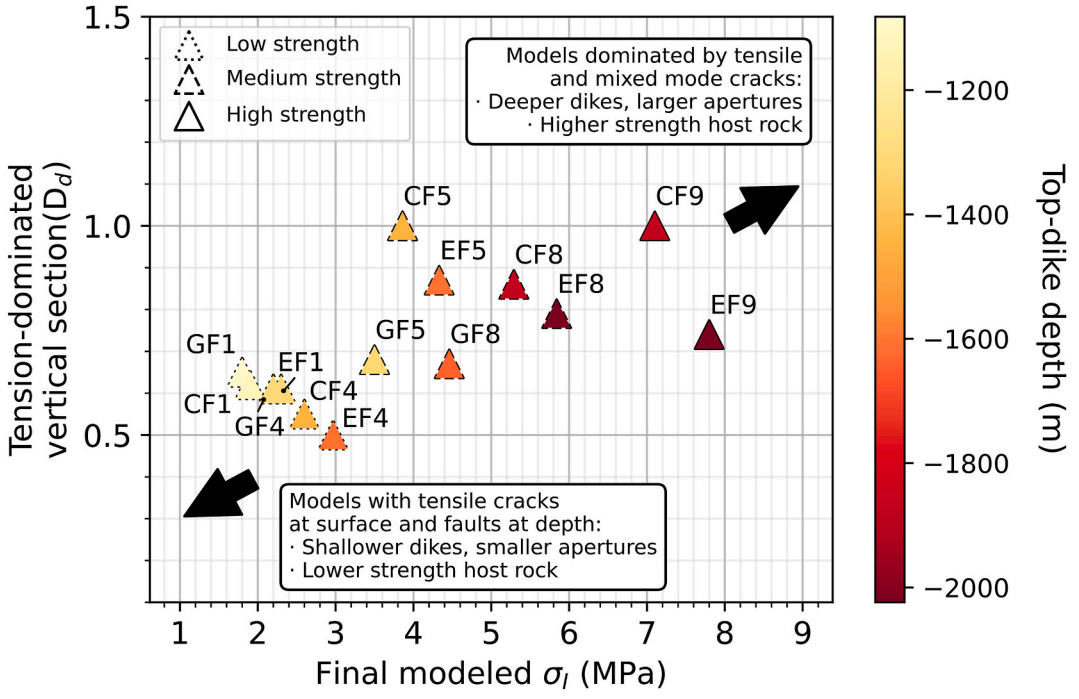

Fig. 6. Proportion of the vertical section between the dike tip and the surface dominated by tensile cracks expressed as a fraction of dike depth (D_d), as function of the final modeled driving stress (σ_I), for all the models defined as compatible with graben nucleation above the dikes. The outline of the triangles represents the quality of the mechanical properties, and their color fill is top dike depth. Tension-dominated models appear at higher driving stresses, greater depths, and stronger host rocks. Models in which tension and dip-slip failure are more evenly distributed correspond to lower driving stresses, shallower depths, and less compliant host rocks. (For interpretation of the references to color in this figure legend, the reader is referred to the Web version of this article.)

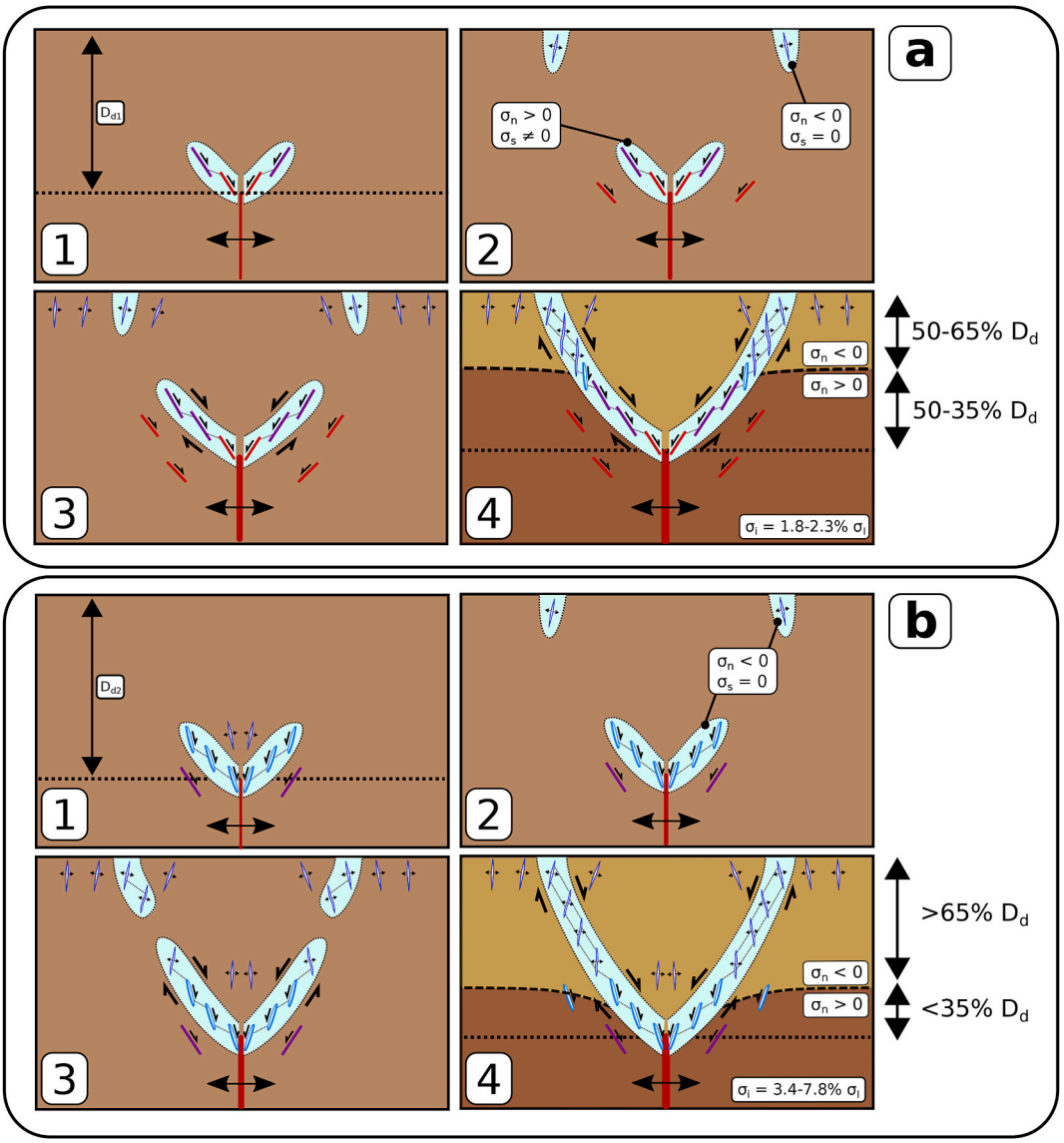

Fig. 7. Conceptual models of the failure sequence which leads to the nucleation of normal faults above an opening dike at different depths ($D_{d1}<D_{d2}$) and in host rocks with different properties. Discontinuity types are represented as in Fig. 4 a) Conceptual model 1 of a shallow dike intruding a moderately competent host rock. In the final step, linkage is established at a relatively low % σ_I. the yellow area, whilst in the dark brown region $\sigma_n > 0$. The thin dotted lines between discontinuities represent the P-type Riedel structures discussed in the text. The regions within the blue polygons are those through which faults eventually nucleate. Discontinuities formed outside these regions may still form but are not presumed to contribute to fault nucleation. (For interpretation of the references to color in this figure legend, the reader is referred to the Web version of this article.)

between deep and shallow systems occurs, which is as low as 0.01 in model CF1 (Table 1). In contrast, for deep dikes, a greater compressive stress acting against a comparatively smaller driving stress results in a shift of the principal stresses toward positive values, which favors the formation of tension-compression and even tensional discontinuities near the dike tip. These are the potential points for the nucleation of later normal faults, which coupled with tensile stresses at the appropriate surface location lead to compatible models (e.g., models EF8 or CF9). In these cases a greater proportion of the vertical section between the dike and the surface is dominated by either tensile or mixed-mode cracks. Because of the larger emplacement depth, a larger modeled σ_I is needed to produce the required sequence of failure (6–7.8 MPa for models with $\beta = 65°$, versus 3.77–4.74 MPa for models with $\beta = 55°$). In summary, a larger aperture and a deeper dike are required in a high-compliance host to produce a failure sequence which favors graben nucleation through mostly tensile discontinuities.

We use the proportion of the tension-dominated vertical section as a function of driving stress in the final step of the compatible models to illustrate and summarize the range of conditions under which compatible models exist (Fig. 6). The tension-dominated axis illustrates the dominant failure mode in the models, whilst the driving stress is useful as it acts as a proxy for dike aperture and mechanical properties (see equation (2)). Shallow dikes in lower strength host rocks need low final modeled driving stresses to produce compatible failure sequences with both joints and faults (Fig. 6, left side). This is because at shallow depths the dike needs to open less (i.e., exert a smaller driving stress) to counterbalance the smaller lithostatic stresses. When failure occurs, it does it in conditions which favor tensional structures closer to the surface and structures with dip-slip at depth. When embedded in a strong host rock, shallow dikes do not favor the nucleation of faults. Oppositely, deep dikes in higher strength host rocks need larger driving stresses to produce a compatible failure sequence dominated by tensile structures (Fig. 6, right side). This occurs due to the opposite reasons. The dikes need to open comparatively more (i.e., exert a larger driving stress), to

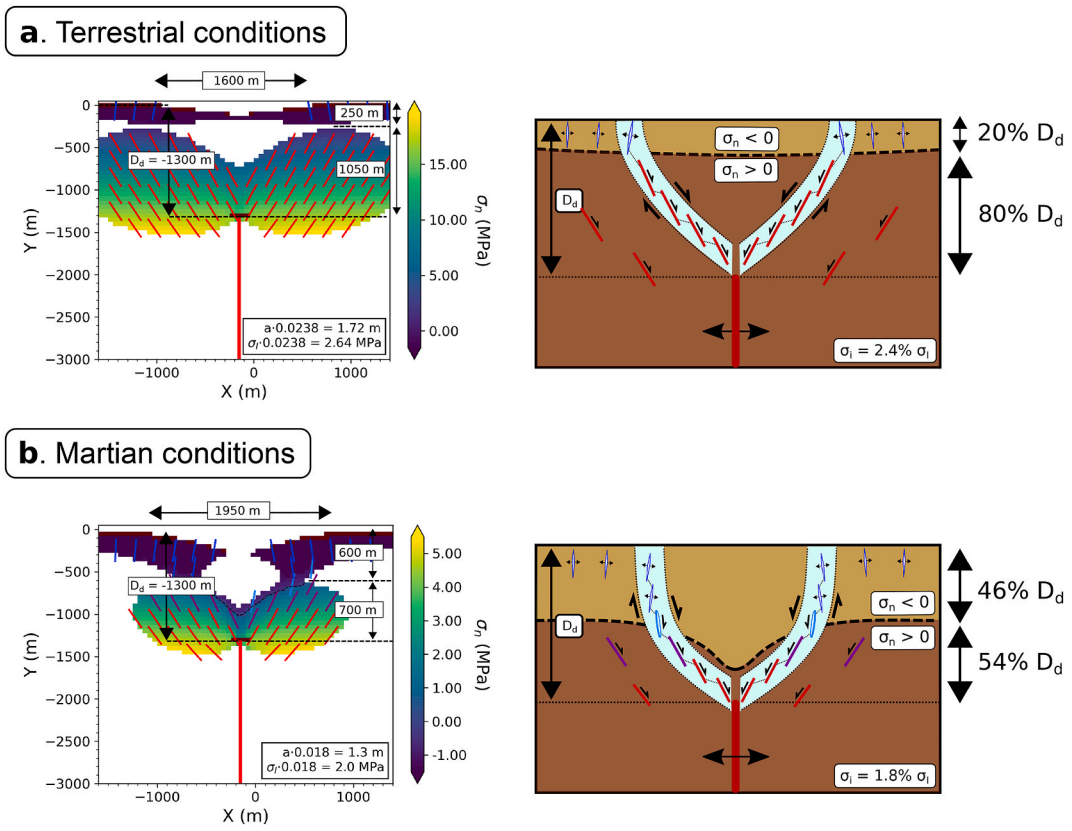

Fig. 8. Comparison between dynamic models ran using the same input parameters (E = 50 GPa, v = 0.25, ρ = 2900 kg m^{-3}, T = 2.5 MPa, μ = 0.58, D_d = −1300, a = 72m) in Martian and terrestrial conditions. a) Terrestrial case. Left: model output with g = 9.8 ms^{-2}. Here the model is run until 2.38% σ_I. Right: Conceptual model of the geometry of the linked discontinuities. b) Martian case. Left: model output with g = 3.7 ms^{-2}. In this case, the model is run until 1.8% σ_I, when linkage occurs. Right: Model of the possible final geometry of the linked discontinuities. In the final dynamic model images (7a and b, left) the depth of the dike (D_d), the vertical section occupied by mode-I and mode-II discontinuities, and the horizontal spacing between the first tension cracks at surface, are indicated. In the conceptual models (8a and b, right) the color schemes are the same as used in Fig. 7. (For interpretation of the references to color in this figure legend, the reader is referred to the Web version of this article.)

counteract larger lithostatic stresses. When failure occurs, it does so under conditions which favor high-angle tensile structures rather than dip-slip normal faults under general compression. When intruding a weaker host rock, the mode of discontinuities and their location is unlikely to favor the nucleation of normal faults. Therefore, there are two general scenarios which may favor the nucleation of normal faults above dikes, from which we propose two general conceptual models.

4.2. *Conceptual models of dike-induced graben nucleation*

Based on the compatible models and the understanding of the physical processes behind them, we propose two general models for the nucleation of normal faults above dikes during the early stages of intrusion, corresponding to the two ends of the spectrum of compatible models (Fig. 7).

In the first, which corresponds to dikes intruded at shallower depths in softer rocks, effective fault linkage and propagation from the dike tip toward the surface and connection to shallow tensile cracks is the key process (Fig. 7a). In these models, mode-II discontinuities formed above the dike tip connect with progressively shallower shears, as the principal stresses move from general compression immediately above the dike tip to tension-compression closer to the surface (Fig. 7a, Steps 1 to 3). At the same time, subvertical tensile cracks formed at the surface, at locations which are compatible with the faults observed at present day, propagate toward depth (Fig. 7a, Steps 2 to 4). Eventually these two systems link, possibly through mixed-mode discontinuities, at depths between 50 and 65% of the total dike depth (Fig. 7a, Step 4). This results in faults with a listric or arcuate shape, steeper at the surface, even outward dipping, and with smaller dip angles at depth. The final linkage of the generated discontinuities leading to rupture and fault generation takes place following two different evolutions depending on the damage zone position. On one hand, the tensile cracks (mode I) are arranged in an en-echelon pattern at approximately 45° of the damage band in the upper part of the model. The linkage of these open cracks propagates downwards necessarily through the generation of Riedel P-type fractures (Fossen, 2016) not reproduced by our elastic-frictional models. On the other, the damage bands generated on both sides of the dike tip are characterized by en-echelon patterns of normal faults (mode II) at 15° from the lobe's main orientation. This en-echelon discontinuities can be interpreted as R-type Riedel (Fossen, 2016) synthetic subsidiary shear fractures that necessarily coalesce into an upward-propagating, low-angle listric normal fault through the linkage of P-type fractures not reproduced by our elastic-frictional models.

In the second scenario, which corresponds to dikes intruded at greater depths in more compliant rocks, propagation of tensile cracks from the surface and their collapse into high-dip normal faults is the key mechanism (Fig. 7b). In these models, mixed-mode and tensile cracks form early both above the dike tip and later close to the surface (Fig. 7b, Steps 1 and 2). More joints continue to grow from depth to the surface and vice versa, and simultaneously throughout the surface (Fig. 7b, Step 3). Some of these joints may already collapse and develop dip-slip surfaces, which aid in the later nucleation of normal faults. Rapid growth of these discontinuities from the surface, which may be joints or incipient fault surfaces, eventually leads to linkage with the deeper mixed-mode

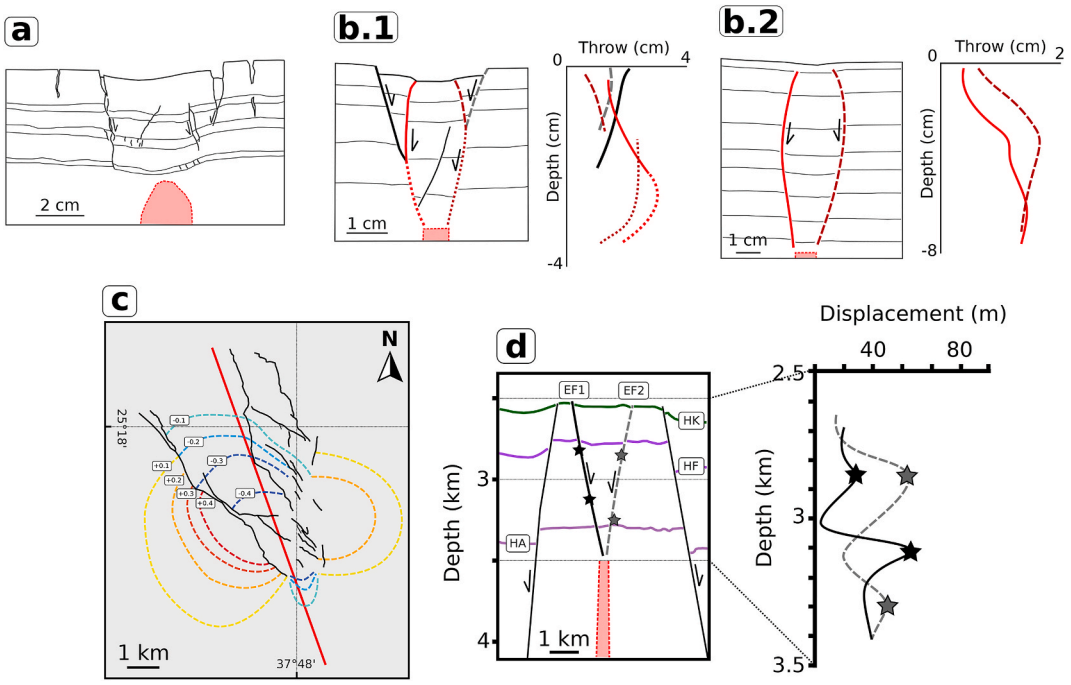

Fig. 9. Compilation of scaled laboratory experiment results and observations of terrestrial dike-induced structures. a) Final model geometry obtained in the experiments by Mastin and Pollard (1988). b) Final model geometry obtained in experiments of dike intrusion with a rectangular upper tip for a medium-depth dike (b.1), and a deep dike (b.2). The corresponding throw profiles for each main fault are shown to the right of each model. Redrafted from Trippanera et al. (2019). c) Schematic representation of the surface structures (faults and open fractures, solid black lines) generated during the Harrat Lunnayir intrusion. The color contours indicate the approximate vertical displacement measured during the episode, as measured by InSAR data. The solid red line is the approximate location of the dike. Based on maps in Trippanera et al. (2019) and Xu et al. (2016). d) Example of Dike-induced faults in the Exmouth Dike Swarm (vertical exaggeration x 5.5) and their corresponding displacement profiles. Stars indicate the displacement maxima. Based on figures in Magee and Jackson (2021). (For interpretation of the references to color in this figure legend, the reader is referred to the Web version of this article.)

shears, at depths >65% of the dike depth (Fig. 7b, Step 4). The result is arcuate faults which may be subvertical or slightly outward dipping at the surface, and lower dips at depth owing to the early development of tensile and mixed mode I-II cracks. An interesting implication of the development of early tensile cracks near the dike tip is that these conditions may somewhat favor the upward propagation of the dike, instead of faulting. In this case, this second model may eventually converge to a similar scenario as in the first conceptual model. In our proposed model the result is similar to the previous case, but the faults would show higher average dips due to the dominance of vertical tensile fracturing. Additionally, in these models the entire region above the dike tip is subject to significant tension with $\sigma_3 < 0$. The final rupture of the damage zone in this case (Fig. 7b) is similar to the upper part of the first model (Fig. 7a), and occurs through the linkage of an en-echelon pattern of open tensile cracks via the necessary generation of P-type Riedel shear fractures not reproduced by our elastic-frictional models.

4.3. Results under Martian vs terrestrial conditions

The processes and conceptual models described so far are valid for models under Martian conditions, i.e., where g = 3.7 m s^{-2}. We ran a model identical to that shown in Fig. 4 using terrestrial g = 9.8 m s^{-2}, to explore general differences between the failure sequences in both settings (Fig. 8).

For the terrestrial case (model E, Fig. 8a), the first discontinuities are faults near the dike tip formed under general compression at <1% σ_I. These continue to grow above and at the sides of the dike in two symmetric lobes, as in many other models. Near-surface tension cracks form at 1.43% σ_I and quickly propagate throughout the surface but not at depth. Linkage between the near-surface cracks and faults at depth occurs at an evolved state of the model at 2.4% σ_I and at a shallow depth of 250 m. Thus, in the final stage of the model tensile cracks are dominant in 20% of the vertical section from the surface to the dike tip.

There are several key differences between the terrestrial and the equivalent Martian case (model M, Fig. 8b). In the former, the % σ_I at which the successive steps occur is greater, mixed-mode discontinuities and faults under tension-compression are mostly absent, the values of σ_n at which failure occurs are larger, the section dominated by tension cracks and faults is much narrower, and the general stress-state is dominated by general compression. The terrestrial g causes the lithostatic stress to be increased approximately three-fold, which increases the weight of the first term in equations (5) through (7). In turn, this results in more positive principal stresses which shift the stress state at any given point towards compression, i.e., modes 3 and 4 in Fig. 4 become more common. $\sigma_3 > 0$ over most of the section, and the magnitude of the normal stress in the failure planes becomes larger. Ultimately, this manifests as faults being predominant over 80% of the section between the surface and the dike, whilst tension cracks dominate over only 20% of the section (Table 1, Fig. 8a). On Mars, the tension-dominated vertical section in the compatible models ranges between 50 and 100% D_d (Table 1, Fig. 6, 46% D_d in the model in 8b), whilst the fault-controlled section is always <50% D_d (Table 1, Fig. 6, 54% D_d in the model in 8b). Thus, dike-induced tension should be expected to be, in general, more dominant on Martian relative to terrestrial dike intrusions. This may have favored the development of large fracture networks above the dikes which would have facilitated fluid circulation. These could have contributed to feed massive fissure eruptions (Vaucher et al., 2009; Wilson et al., 2009), generated locations for and promoted the accumulation of ores as those found in massive sulfide or iron oxide-copper-gold deposits related to mafic magmatism (Lewis, 1955; Keays, 1987; Ernst and Jowitt, 2013; Jowitt and Ernst, 2016), or created transient hydrothermal systems which developed conditions of habitability (Craft and Lowell, 2012; Craft, 2013; Costello et al., 2020).

4.4. Comparisons with scaled laboratory experiments

The results of several dike intrusion laboratory experiments can be interpreted and explained in terms of our model parameters, which supports their consistency. However, comparing the result of these models with our results must be done with caution since all scaled laboratory experiments are done inherently under terrestrial conditions.

Mastin and Pollard (1988) simulated a granular medium in which they modeled dike intrusion introducing cardboard sheets through a sleeve at the model base. In their model, subvertical tensile cracks developed at the surface to the sides of the dike and propagate inward. Joints continue to form at depth, some of which eventually collapsed and developed dip-slip fault surfaces (Fig. 9a). This is similar to the proposed evolution of our generic model 2. A significant difference is, however, that their models lack any significant failure close to the dike tip. A possible explanation for this is that they modeled a very shallow dike. This greatly increases the contribution of the dike-induced tension for any given aperture, resulting in the dominance of joints above the dike. This is very similar to models such as 8 or 9 in all three sites, which are dominated by tension cracks and lack shear structures at depth (Supplementary Material).

Trippanera et al. (2014) modeled dike intrusion by inserting up to 20 0.5-mm thick metal plates in a cohesive sand to a depth of 4 cm below the model surface. In their models 1 cm ≡ 100 m, and thus the thickness intruded in the early stages (e.g., their Fig. 3d) is equivalent to a 3 m dike at a depth of 400 m. In their model, shear discontinuities were first formed close to the dike tip which propagated toward the surface, as proposed in our generic model 1. However, although surface tensile fracturing occurred at the sides of the dike, these did not grow to depth and linked to shear cracks. Instead, the early-formed faults grew to the surface as outward dipping faults. Since the scaled mechanical properties of their model are not known precisely, the lack of tensile cracks in their model may be attributed to the greater contribution of remote compressive stresses, which is expected in models under terrestrial conditions. In a subsequent work, Trippanera et al. (2016) simulated thickening dike intrusions of up 100 m to depths between 100 and 800 m (assuming the same scaling as in their previous paper) in a cohesive medium with frictional properties C = 10 MPa and μ' = 0.7. Their model with rectangular dike tips at shallow depths is dominated by the quick development of dip-slip surfaces from which normal faults grow. In their medium-depth model, surface tension cracks are more abundant and the final graben is composed of a set of outer inward-dipping normal faults, which grow from surface to depth as indicated by the throw profiles, and another of inner arcuate outward-dipping faults, which grow from depth to surface (Fig. 9b1). In the deep model, a single pair of arcuate faults grows from the dike tip to the surface (Fig. 9b2). Although they do not report this, it is likely that the highly dipping faults result from the coalescing of tensile cracks in the early model stages, which would resemble our conceptual model 2. In both the experiments and our models, the development of high-dip arcuate faults is favored by a relatively high tensile strength. In our models, this is further favored by the greater weight of the dike-induced stress under Martian conditions, whilst in their experiments this is caused by the greater apertures (up to 100 m) which model a higher driving stress in a relatively compliant rock. Indeed, tests of deep dikes (>1 km) with larger apertures (≈10 m) under terrestrial conditions and the same frictional properties as in these experiments yield results like models GF5, EF5, or CF5 (Supplementary Material).

One key limitation of both laboratory experiments is that they reproduced the injection of a viscous liquid through the intrusion of solid slabs into low-cohesion granular media. Firstly, the use of solid plates more closely models the inflation of a pre-existing dike, or successive intrusions in a dike core complex, and not the initial opening of a crack via fluid pressure. Secondly, silica sand is a very low cohesion material which appropriately models very low strength host rocks, i.e., weakened, altered, or loose lithologies, but not intact well consolidated sedimentary rocks, or crystalline volcanic or metamorphic terrains. Thus, the low cohesion of the models' material may explain the absence of significant tensile failure. However, laboratory experiments which simulate dike intrusion though the injection of a viscous fluid in a cohesive granular media, and thus more accurately model the physical intrusion process, do not produce normal faults (Abdelmalak et al., 2012; Poppe et al., 2019; Bertelsen et al., 2021). Instead, a dome bound by sets of reverse faults is formed at the surface above the dike. Therefore, they cannot be readily compared with the results presented in this work. Interestingly, this is similar to the results of the DEMs in Wyrick and Smart (2009), which also failed to produce graben at surface. In similar numerical models Hardy (2016) concluded that Wyrick and Smart (2009) had not produced any graben at surface due to the imposition of a basal detachment in a confined model setup. The same or a similar reason may explain why the former experiments did not produce graben. These difficulties in dike laboratory experiments should be further investigated to find fully appropriate setups to model dike intrusions, which can be then reconciled with field observations and numerical models such as those presented in this work.

4.5. Comparisons with observed dike-induced deformation

The results of our models are also consistent with field observations of structures generated during recent diking episodes and with dike-induced faults as mapped in seismic reflection data.

The Harrat-Lunnayir (HL) 2009 diking episode, for example, can be reasonably compared with some of our models. During this episode a dike of up to 4 m aperture intruded to depths of 1–2 km generating a graben of 2–7 km width (Pallister et al., 2010). Faults with dip-slip and open fractures with vertical and horizontal offsets have been mapped at a distance of 1–3.5 km relative to the modeled dike (Fig. 9c, Trippanera et al., 2019). In our Martian examples, the selected Cerberus Fossae graben has a surface width of approximately 2.1 km, like the SE section of the HL system. Assuming a 65° fault dip and a relatively compliant host rock (e.g., model CF8), we obtain a top dike depth of −1.6 km and tension cracks appear at 1.1 km relative to the dike. This, however, occurs at a larger dike aperture of 18 m, which is required in a model with relatively low E (7.5 GPa) to produce a sufficient driving stress of 4.4 MPa that causes failure at surface, as per equation (2). However, given an E = 30 GPa and v = 0.25 (therefore μ = 12 GPa), which may be appropriate for the Neoproterozoic basement in the Nubian shield, 4.4 MPa would require an opening of only ≈ 2.4 m, which more closely resembles the estimated aperture of the HL dike. Even smaller apertures would be required for a dike embedded in a host rock subject to remote extension, as may be the case of dikes emplaced in divergent margins. The distribution of stresses and the location of the maximum tension is independent of g and therefore this comparison is possible.

Dike-induced faults mapped in seismic data show geometries and displacement profiles which are compatible with our proposed models (Fig. 9d). Detail 3D seismic surveys of the Exmouth Basin (NW offshore Australia) frequently show two discrete faults formed on top of dikes intruding a Mesozoic sedimentary sequence (Magee and Jackson, 2020). Moreover, faults occasionally have subvertical dips near the syn-faulting free surface, and therefore a listric or arcuate geometry. Additionally, Magee and Jackson (2021) mapped horizons affected by dike-induced faults and identified, in certain faults, two displacement maxima (Fig. 9d). This is explained by the faults nucleating at two different points and eventually linking to form a single surface. Interestingly, this is the same evolution as in the medium-depth models in Trippanera et al. (2016). In our conceptual models we propose the coeval growth of discontinuities from the surface to depth and vice versa, and thus fault nucleation from two locations, in agreement with some of the seismically mapped displacements.

4.6. Future steps in dike-induced graben modeling

Our models are only valid for the earliest stages of diking and graben nucleation and cannot explain later fault growth or the accumulation of subsidence after diking. The investigated graben in the Elysium region, hypothesized to be dike-induced, have depths of up to 760 m. In contrast, and to cite a few examples, the Harrat-Lunnayir 2009 episode produced an initial graben with a maximum depth of 0.8 m (Baer and Hamiel, 2010), the Afar 2005 event caused a subsidence of 2–3 m in the northern rift segment (Wright et al., 2006), and the Bárðarbunga-Holuhraun (BH) dike generated a maximum vertical displacement within the graben of 6 m (Ruch et al., 2016). Therefore, if the Elysium graben are dike-induced, early faulting and its related subsidence is insufficient to explain their great depths. Our models cannot address this issue but current research already begins to shed light on the subject. Kolzenburg et al. (2021) have reported that the subsidence in the BH graben is very stable, experiencing little to no post-diking sinking. Oppositely, Nobile et al. (2020) have identified substantial aseismic post-diking sinking in the Harrat-Lunnayir structures, of up to 4 mm/yr. Both magma contraction during dike cooling and slow gravitational collapse of the dike-induced faults may contribute to post-intrusion subsidence. For dikes with thicknesses between 60 and 900 m, cooling times may be between 65 and 15000 years (using the conductive cooling theory in Rubin, 1995, and assuming the rest of parameters required as therein). However, several studies have shown that dike contraction for meters-thick dikes it is limited to cm, and that it occurs mainly at its center (Daniels et al., 2012; Loncar and Huppert, 2022). Therefore, aperture reduction due to cooling in dikes with apertures from meters to hundreds of meters should be limited to a few meters. Consequently, cooling-related contraction is relatively limited in time, and insufficient in magnitude to account for the observed present-day subsidence. Oppositely, prolonged normal fault collapse may be a better alternative to explain post-diking subsidence. The immediate displacements generated by dike-induced faults do not correspond to the values expected for faults which are at least tens of kilometers long, as shown by terrestrial examples. For example, the total length of the fault segments measured by Trippanera et al. (2019) at Harrat-Lunnayir is of approximately 9.2 km, whilst the largest vertical offset measured is of 4.5 m. In terms of displacement-length (D-L) scaling, these faults are deficient in displacement, and should accumulate slip and grow to match with known D-L trends for fully developed normal faults (e.g., Cowie and Scholz, 1992; Kim and Sanderson, 2005; Nicol et al., 2005; Schultz et al., 2006). If the same is the case in the Elysium graben, movement must have continued long after intrusion. Although slip rates in dike-induced normal faults are largely unknown, if assuming the same long term rates as in well-studied faults in active extensional settings these may be between 0.01 and 3.5 mm/yr (Nicol et al., 2005, 2010; McClymont et al., 2009; Mouslopoulou et al., 2009; Alfaro et al., 2021). Interestingly, the upper boundary of this range is similar to the post-diking subsidence estimated by Nobile et al. (2020) in the Harrat-Lunnayir system. Under the assumption that the dikes intruded in a single episode and a steady post-diking subsidence at a maximum rate of 4 mm/yr, the graben in the Elysium Mons area may have taken between 20 and 190 ka to reach their current depths. Most of the recent volcanic activity in the Elysium province has been dated between 0.5 and 2 Ma (Vaucher et al., 2009; Platz and Michael, 2011; Pasckert et al., 2012). More specifically, low-albedo streaks and mantles associated to Cerberus Fossae fissures have been identified as pyroclastic deposits associated to extremely recent fissure eruptions dated between 46 and 222 ka (Roberts et al., 2007; Andrews-Hanna, 2017; Horvath et al., 2021). Therefore, diking events taking place some time in the last 190 ka would be fully consistent with our current understanding of tectonomagmatic activity in the region. Consequently, episodic gravitational collapse of the faults after diking is a plausible mechanism to explain the present-day subsidence observed in the Martian graben.

Models which can simulate long-term post-diking faulting and subsidence are needed to understand how terrestrial and Martian dike-induced graben are formed. This process will likely involve both aseismic and seismic faulting after diking. Seismic events with magnitudes between <1 and 4 have been recently detected by the InSight probe (Giardini et al., 2020; Brinkman et al., 2021). Some of the larger marsquakes have been located in the vicinity of Cerberus Fossae, and the smaller events detected in the upper crust, which location cannot be determined, may be associated to minor fault ruptures related to long-term post-diking subsidence, or other dike-related structures (Stähler et al., 2022). On Earth, investigating these processes is relevant to fully understand seismic hazards in regions which may have been affected by diking episodes in the recent past. Models of fault rupture and graben subsidence after diking may shed light on the magnitudes and specific characteristics of post-diking seismicity, with applications to terrestrial environments and to improve our understanding of the processes occurring in other planetary lithospheres.

5. Conclusions

We investigated the processes of discontinuity nucleation and early evolution of the graben-bounding normal faults induced above vertical dike intrusions through elastic-frictional models. We applied this modeling to understand three graben with distinct geometries in the Elysium volcanic province which are all hypothesized to host dikes at depth. At each site we modeled the dikes and dike-induced stresses with different mechanical and frictional parameters to understand possible mechanisms of graben nucleation under Martian conditions.

The models show two scenarios which are compatible with graben geometry as we infer it at present-day, from which we propose two conceptual models of dike-induced graben nucleation. The first model involves shallow, narrow dikes hosted in a low compliance host rock. In this case, nucleation occurs through mode II discontinuities which propagate from the dike tip to the surface and connect with shallow mode I cracks. In this model, these dominate over 50–65% of the vertical section between the surface and the dike (D_d), with faults occupying 35–50% of D_d. The second model involves deep wide dikes in higher compliance host rocks. In this scenario, propagation of mode I cracks from the surface and their collapse into high dip mode II faults is the most relevant process. In these cases, tensile structures occupy between 50 and 100% of D_d, whilst faults are present over less than 34% of the section. The results of our models are compatible with laboratory experiments of dike intrusion, dike-induced deformation observed in recent diking episodes, and with seismically mapped faults, which support their consistency.

We also performed two equivalent models under Martian and Terrestrial conditions to compare their evolution. We conclude that graben nucleation on Mars is likely to be dominated by failure under tension-compression and tension over a greater extent of the vertical section, ought to the greater weight of the dike-induced stresses under a smaller gravitational load. Therefore, the corresponding normal faults should be expected to have larger average dip angles, and host complex open fracture systems between the surface and the dike tip. Oppositely, dike deformation in terrestrial settings is more likely to be dominated by faulting under general compression and show narrower tension-dominated regions closer to the surface.

Therefore, our models, which combine geometrically-obtained dike parameters and theory of fracture and frictional mechanics, provide plausible nucleation mechanisms of dike-induced graben consistent with both laboratory experiments and observations. This conforms a general theory of dike-induced failure in host rocks with varying elastic-frictional properties, which is critical to understand the early development of dike-related faults. However, they are only the first step to fully understand the evolution of giant deep dike-related graben, which is of key relevance to understand post-diking terrestrial deformation, and current seismicity in tectonically active regions of Mars such as Cerberus Fossae.

Author statement

Sam Rivas-Dorado: Conceptualization, Methodology, Software, Validation, Investigation, Data Curation, Visualization, Writing - Original Draft, Writing - Review & Editing, **Javier Ruiz**: Conceptualization, Writing - Review & Editing, Supervision, **Ignacio Romeo**: Conceptualization, Visualization, Writing - Review & Editing, Supervision, Funding acquisition.

Declaration of competing interest

The authors declare that they have no known competing financial interests or personal relationships that could have appeared to influence the work reported in this paper.

Data availability

The DiES code is available at https://github.com/SamRivasDorado/DiES

Acknowledgements

This research was funded by project TECTOMARTE, PGC 2018-095340-B-I00 (Spanish Ministry of Science, Innovation and Universities). The authors would like to thank the Editor, Fabrizio Agosta, and reviewer, Sam Poppe, for their encouraging and thorough reviews, which greatly improved the quality of this paper. Sam Rivas-Dorado would like to thank Paul Segall and the members of the Stanford Volcanology Seminar for many fruitful discussions about volcanology during the year 2021–2022, in which this paper was written.

Appendix A. Supplementary data

Supplementary data to this article can be found online at https://doi.org/10.1016/j.jsg.2022.104778.

References

Abdelmalak, M.M., Mourgues, R., Galland, O., Bureau, D., 2012. Fracture mode analysis and related surface deformation during dyke intrusion : results from 2D experimental modelling. Earth Planet Sci. Lett. 359 (360), 93–105. https://doi.org/10.1016/j.epsl.2012.10.008.

Alfaro, P., Sánchez-Alzola, A., Martin-Rojas, I., García-Tortosa, F.J., Galindo-Zaldívar, J., Avilés, M., Garrido, A.C.L., de Galdeano, C.S., Ruano, P., Martínez-Moreno, F.J., Pedrera, A., Lacy, M.C., Borque, M.J., Medina-Cascales, I., Gil, A.J., 2021. Geodetic fault slip rates on active faults in the Baza sub-Basin (SE Spain): insights for seismic hazard assessment. J. Geodyn. 144 https://doi.org/10.1016/j.jog.2021.101815.

Andrews-Hanna, J.C., 2017. A very recent pyroclastic eruption from the Cerberus Fossae on Mars. Lunar and Planetary Science XLVIII.

Apuani, T., Corazzato, C., Cancelli, A., Tibaldi, A., 2005. Physical and mechanical properties of rock masses at Stromboli: a dataset for volcano instability evaluation. Bull. Eng. Geol. Environ. 64, 419–431. https://doi.org/10.1007/s10064-005-0007-0.

Ayele, A., Keir, D., Ebinger, C., Wright, T.J., Stuart, G.W., Buck, W.R., Jacques, E., Ogubazghi, G., Sholan, J., 2009. September 2005 mega-dike emplacement in the Manda-Harraro nascent oceanic rift (Afar depression). Geophys. Res. Lett. 36, 1–5. https://doi.org/10.1029/2009GL039605.

Baer, G., Hamiel, Y., 2010. Form and growth of an embryonic continental rift: InSAR observations and modelling of the 2009 western Arabia rifting episode. Geophys. J. Int. 182, 155–167. https://doi.org/10.1111/j.1365-246X.2010.04627.x.

Bertelsen, H.S., Guldstrand, F., Sigmundsson, F., Pedersen, R., Mair, K., Galland, O., 2021. Beyond elasticity: are Coulomb properties of the Earth's crust important for volcano geodesy? J. Volcanol. Geoth. Res. 410, 107153 https://doi.org/10.1016/j.jvolgeores.2020.107153.

Bieniawski, Z.T., 1984. Rock Mechanics Design in Mining and Tunneling (Rotterdam).

Brinkman, N., Stähler, S.C., Giardini, D., Schmelzbach, C., Khan, A., Jacob, A., Fuji, N., Perrin, C., Lognonné, P., Beucler, E., Böse, M., Ceylan, S., Charalambous, C., Clinton, J.F., van Driel, M., Euchner, F., Horleston, A., Kawamura, T., Knapmeyer-Endrun, B., Mainsant, G., Panning, M.P., Pike, W.T., Scholz, J., Robertsson, J.O.A., Banerdt, W.B., 2021. First focal mechanisms of marsquakes. J. Geophys. Res.: Planets. https://doi.org/10.1029/2020je006546.

Burr, D.M., McEwen, A.S., Sakimoto, S.E.H., 2002. Recent aqueous floods from the Cerberus fossae, Mars. Geophys. Res. Lett. 29, 1–5. https://doi.org/10.1029/2001GL013345.

Cassanelli, J.P., Head, J.W., 2018. Large-scale lava-ice interactions on Mars: investigating its role during late amazonian central Elysium planitia volcanism and the formation of Athabasca Valles. Planet. Space Sci. 158, 96–109. https://doi.org/10.1016/j.pss.2018.04.024.

Chadwick, D.J., Lucchitta, B.K., 1993. Fault geometries and extension in the Valles marineris. Mars. 24th LPSC 263–264.

Chamberlin, R.T., 1910. The appalachian folds of central Pennsylvania. J. Geol. 18, 228–251. https://doi.org/10.1086/621722.

Chamberlin, R.T., Salisbury, R., 1909. Geology: V1-Geologic Processes and Their Results. Henry Holt and Company, New York.

Clifton, A.E., Schlische, R.W., 2001. Nucleation, growth, and linkage of faults in oblique rift zones: results from experimental clay models and implications for maximum fault size. Geology 29, 455–458. https://doi.org/10.1130/0091-7613(2001)029<0455:NGALOF>2.0.CO;2.

Costello, L.J., Filiberto, J., Crandall, J.R., Potter-McIntyre, S.L., Schwenzer, S.P., Miller, M.A., Hummer, D.R., Olsson-Francis, K., Perl, S., 2020. Habitability of hydrothermal systems at Jezero and Gusev Craters as constrained by hydrothermal alteration of a terrestrial mafic dike. Chem. Erde 80, 125613. https://doi.org/10.1016/j.chemer.2020.125613.

Cowie, P.A., Scholz, C.H., 1992. Displacement-length scaling relationship for faults: data synthesis and discussion. J. Struct. Geol. 14, 1149–1156. https://doi.org/10.1016/0191-8141(92)90066-6.

Craft, K.L., 2013. Dike-driven Hydrothermal Processes on Mars and Sill Emplacement on Europa.

Craft, K.L., Lowell, R.P., 2012. Boundary layer models of hydrothermal circulation on Mars and its relationship to geomorphic features. J. Geophys. Res.: Planets 117. https://doi.org/10.1029/2012JE004049.

Daniels, K.A., Kavanagh, J.L., Menand, T., Sparks, R.S.J., 2012. The shapes of dikes: evidence for the influence of cooling and inelastic deformation. Bull. Geol. Soc. Am. 124, 1102–1112. https://doi.org/10.1130/B30537.1.

Ebinger, C.J., Casey, M., 2001. Continental breakup in magmatic provinces: an Ethiopian example. Geology 29, 527–530. https://doi.org/10.1130/0091-7613(2001)029<0527:CBIMPA>2.0.CO;2.

Ernst, R., Jowitt, S., 2013. Large Igneous Provinces (LIPs) and Metallogeny. Society of Economic Geologists, Inc., pp. 17–51

Fossen, H., 2016. Structural Geology, second ed. Cambridge University Press, New York.

Gallagher, C., Balme, M., Soare, R., Conway, S.J., 2018. Formation and degradation of chaotic terrain in the Galaxias regions of Mars: implications for near-surface storage of ice. Icarus 309, 69–83. https://doi.org/10.1016/j.icarus.2018.03.002.

Giardini, D., Lognonné, P., Banerdt, W., Pike, W., Christensen, U., Ceylan, S., Clinton, J., Driel, M. van, Stähler, S., Böse, M., Garcia, R., Khan, A., Panning, M., Perrin, C., Banfield, D., Beucler, E., Charalambous, C., Euchner, F., Horleston, A., Jacob, A., Kawamura, T., Kedar, S., Mainsant, G., Scholz, J.-R., Smrekar, S., Spiga, A., Agard, C., Antonangeli, D., Barkaoui, S., Barrett, E., Combes, P., Conejero, V., Daubar, I., Drilleau, M., Ferrier, C., Gabsi, T., Gudkova, T., Hurst, K., Karakostas, F., King, S., Knapmeyer, M., Knapmeyer-Endrun, B., Ljorca-Cejudo, R., Lucas, A., Luno, L., Margerin, L., McClean, J., Mimoun, D., Murdoch, N., Nimmo, F., Nonon, M., Pardo, C., Rivoldini, A., Manfredi, J.A.R., Samuel, H., Schimmel, M., Stott, A.E., Stutzman, E., Teanby, N., Warren, T., Weber, R., Wieczorek, M., Yana, C., 2020. The seismicity of Mars. Nat. Geosci. 13, 205–212. https://doi.org/10.1038/s41561-020-0539-8.

Goudy, C.L., Schultz, R.A., 2005. Dike intrusions beneath grabens south of Arsia Mons, Mars. Geophys. Res. Lett. 32, 1–3. https://doi.org/10.1029/2004GL021977.

Hardy, S., 2016. Does shallow dike intrusion and widening remain a possible mechanism for graben formation on Mars? Geology 44, 107–110. https://doi.org/10.1130/G37285.1.

Head, J.W., Wilson, L., 1993. Lunar graben formation due to near-surface deformation accompanying dike emplacement. Planet. Space Sci. 41, 719–727. https://doi.org/10.1016/0032-0633(93)90114-H.

Head, J.W., Wilson, L., 1992. Lunar mare volcanism: stratigraphy, eruption conditions, and the evolution of secondary crusts. Geochem. Cosmochim. Acta 56, 2155–2175. https://doi.org/10.1016/0016-7037(92)90183-J.

Head, J.W., Wilson, L., Mitchell, K.L., 2003. Generation of recent massive water floods at Cerberus Fossae, Mars by dike emplacement, cryospheric cracking, and confined aquifer groundwater release. Geophys. Res. Lett. 30 https://doi.org/10.1029/2003GL017135.

Heap, M.J., Wadsworth, F.B., Heng, Z., Xu, T., Griffiths, L., Aguilar Velasco, A., Vairé, E., Vistour, M., Reuschlé, T., Troll, V.R., Deegan, F.M., Tang, C., 2021. The tensile strength of volcanic rocks: experiments and models. J. Volcanol. Geoth. Res. 418, 107348 https://doi.org/10.1016/j.jvolgeores.2021.107348.

Horvath, D.G., Moitra, P., Hamilton, C.W., Craddock, R.A., Andrews-Hanna, J.C., 2021. Evidence for geologically recent explosive volcanism in Elysium Planitia, Mars. Icarus 365, 114499. https://doi.org/10.1016/j.icarus.2021.114499.

Jaeger, J.C., Cook, N.G.W., Zimmerman, R.W., 2007. Fundamentals of Rock Mechanics.

Jaeger, W.L., Keszthelyi, L.P., McEwen, A.S., Dundas, C.M., Russell, P.S., 2007. Athabasca Valles, Mars: a lava-draped channel system. Science 317, 1709–1711. https://doi.org/10.1126/science.1143315.

Jaeger, W.L., Keszthelyi, L.P., Skinner, J.A., Milazzo, M.P., McEwen, A.S., Titus, T.N., Rosiek, M.R., Galuszka, D.M., Howington-Kraus, E., Kirk, R.L., 2010. Emplacement of the youngest flood lava on Mars: a short, turbulent story. Icarus 205, 230–243. https://doi.org/10.1016/j.icarus.2009.09.011.

Jónsson, S., 2012. Tensile rock mass strength estimated using InSAR. Geophys. Res. Lett. 39, 1–5. https://doi.org/10.1029/2012GL053309.

Jowitt, S.M., Ernst, R.E., 2016. Large igneous provinces, their giant mafic dyke swarms, and links to metallogeny. Acta Geol. Sin. 90, 193–194. https://doi.org/10.1111/1755-6724.12968.

Keays, R.R., 1987. Principles of mobilization (dissolution) of metals in mafic and ultramafic rocks - the role of immiscible magmatic sulphides in the generation of hydrothermal gold and volcanogenic massive sulphide deposits. Ore Geol. Rev. 2, 47–63. https://doi.org/10.1016/0169-1368(87)90023-0.

Kim, Y.S., Sanderson, D.J., 2005. The relationship between displacement and length of faults: a review. Earth Sci. Rev. 68, 317–334. https://doi.org/10.1016/j.earscirev.2004.06.003.

Knapmeyer-Endrun, B., Panning, M.P., Bissig, F., Joshi, R., Khan, A., Kim, D., Lekić, V., Tauzin, B., Tharimena, S., Plasman, M., Compaire, N., Garcia, R.F., Margerin, L., Schimmel, M., Stutzmann, É., Schmerr, N., Bozdağ, E., Plesa, A.-C., Wieczorek, M.A., Broquet, A., Antonangeli, D., McLennan, S.M., Samuel, H., Michaut, C., Pan, L., Smrekar, S.E., Johnson, C.L., Brinkman, N., Mittelholz, A., Rivoldini, A., Davis, P.M., Lognonné, P., Pinot, B., Scholz, J.-R., Stähler, S., Knapmeyer, M., van Driel, M., Giardini, D., Banerdt, W.B., 2021. Thickness and structure of the martian crust from InSight seismic data. Science. https://doi.org/10.1126/science.abf8966.

Koehn, D., Steiner, A., Aanyu, K., 2019. Modelling of extension and dyking-induced collapse faults and fissures in rifts. J. Struct. Geol. 118, 21–31. https://doi.org/10.1016/j.jsg.2018.09.017.

Kolzenburg, S., Kubanek, J., Dirscherl, M., Hamilton, C.W., Hauber, E., Scheidt, S.P., Münzer, U., 2021. Solid as a rock: tectonic control of graben extension and dike propagation. Geology. https://doi.org/10.1130/G49406.1.

Kuntz, M.A., Anderson, S.R., Champion, D.E., Lanphere, M.A., Grunwald, D.J., 2002. Tension cracks, eruptive fissures, dikes, and faults related to late Pleistocene-Holocene basaltic volcanism and implications for the distribution of hydraulic conductivity in the eastern Snake River Plain, Idaho. Spec. Pap. Geol. Soc. Am. 353, 111–133. https://doi.org/10.1130/0-8137-2353-1.111.

Lama, R.D., Vutukuri, V.S., 1978. Handbook on Mechanical Properties of Rocks—Testing Techniques and Results, vol. II. Trans Tech Publications, Clausthal.

Lewis, D.V., 1955. Relationships of ore bodies to dikes and sills. Econ. Geol. 50, 495–516.

Loncar, M., Huppert, H.E., 2022. Dyke cooling upon intrusion: subsequent shape change, cooling regimes and the effect of further magma input. Earth Planet Sci. Lett. 593, 117687 https://doi.org/10.1016/j.epsl.2022.117687.

Magee, C., Jackson, C., 2020. Seismic reflection data reveal the 3D structure of the newly discovered Exmouth Dyke Swarm, offshore NW Australia. Solid Earth 11, 579–606. https://doi.org/10.5194/se-11-579-2020.

Magee, C., Jackson, C.A.L., 2021. Can we relate the surface expression of dike-induced normal faults to subsurface dike geometry? Geology 49, 366–371. https://doi.org/10.1130/G48171.1.

Mastin, L.G.L.G., Pollard, D.D., 1988. Surface deformation and shallow dike intrusion processes at inyo craters, long valley, California. J. Geophys. Res. Solid Earth 93, 13221–13235. https://doi.org/10.1029/JB093iB11p13221.

McClymont, A.F., Villamor, P., Green, A.G., 2009. Fault displacement accumulation and slip rate variability within the Taupo Rift (New Zealand) based on trench and 3-D ground-penetrating radar data. Tectonics 28, 1–25. https://doi.org/10.1029/2008TC002334.

McKenzie, D., Nimmo, F., 1999. The generation of martian floods by the melting of ground ice above dykes. Nature 397, 231–233. https://doi.org/10.1038/16649.

Mège, D., Masson, P., 1996. A plume tectonics model for the Tharsis province, Mars. Planet. Space Sci. 44, 1499–1546. https://doi.org/10.1016/S0032-0633(96)00113-4.

Mouslopoulou, V., Walsh, J.J., Nicol, A., 2009. Fault displacement rates on a range of timescales. Earth Planet Sci. Lett. 278, 186–197. https://doi.org/10.1016/j.epsl.2008.11.031.

Muskhelishvili, N.I., 1953. Some Basic Problems of the Mathematical Theory of Elasticity : Fundamental Equations, Plane Theory of Elasticity, Torsion, and Bending.

Nicol, A., Walsh, J., Berryman, K., Nodder, S., 2005. Growth of a normal fault by the accumulation of slip over millions of years. J. Struct. Geol. 27, 327–342. https://doi.org/10.1016/j.jsg.2004.09.002.

Nicol, A., Walsh, J.J., Villamor, P., Seebeck, H., Berryman, K.R., 2010. Normal fault interactions, paleoearthquakes and growth in an active rift. J. Struct. Geol. 32, 1101–1113. https://doi.org/10.1016/j.jsg.2010.06.018.

Nobile, A., Cao, Y., Youssof, M., Trippanera, D., Passarelli, L., 2020. Post-Diking Deformation in Harrat Lunayyir (Saudi Arabia) from InSAR. EGU 2020.

Pallister, J.S., McCausland, W.A., Jónsson, S., Lu, Z., Zahran, H.M., El Hadidy, S., Aburukbah, A., Stewart, I.C.F., Lundgren, P.R., White, R.A., Moufti, M.R.H., 2010. Broad accommodation of rift-related extension recorded by dyke intrusion in Saudi Arabia. Nat. Geosci. 3, 705–712. https://doi.org/10.1038/ngeo966.

Pasckert, J.H., Hiesinger, H., Reiss, D., 2012. Rheologies and ages of lava flows on Elysium Mons, Mars. Icarus 219, 443–457. https://doi.org/10.1016/j.icarus.2012.03.014.

Pedersen, G.B.M., Head, J.W., Wilson, L., 2010. Formation, erosion and exposure of Early Amazonian dikes, dike swarms and possible subglacial eruptions in the Elysium Rise/Utopia Basin Region, Mars. Earth Planet Sci. Lett. 294, 424–439. https://doi.org/10.1016/j.epsl.2009.08.010.

Platz, T., Michael, G., 2011. Eruption history of the Elysium volcanic province, Mars. Earth Planet Sci. Lett. 312, 140–151. https://doi.org/10.1016/j.epsl.2011.10.001.

Pollard, D.D., Delaney, P.T., Duffield, W.A., Endo, E.T., Okamura, A.T., 1983. Surface deformation in volcanic rift zones. Tectonophysics 94, 541–584. https://doi.org/10.1016/0040-1951(83)90034-3.

Pollard, D.D., Martel, S.J., 2020. Structural Geology: A Quantitative Introduction. Cambridge University Press, Cambridge. https://doi.org/10.1017/9781139547222.

Pollard, D.D., Segall, P., 1987. Theoretical Displacements and Stresses Near Fractures in Rock: with Applications to Faults Joints, Veins, Dikes and Solution Surfaces, Fracture Mechanics of Rock. Academic Press Inc., London https://doi.org/10.1016/B978-0-12-066266-1.50013-2.

Poppe, S., Holohan, E.P., Galland, O., Buls, N., Van Gompel, G., Keelson, B., Tournigand, P.Y., Brancart, J., Hollis, D., Nila, A., Kervyn, M., 2019. An inside perspective on magma intrusion: quantifying 3d displacement and strain in laboratory experiments by dynamic X-ray computed tomography. Front. Earth Sci. 7, 1–20. https://doi.org/10.3389/feart.2019.00062.

Rivas-Dorado, S., 2022. DiES (Discontinuities in Elastic Space).

Rivas-Dorado, S., Ruiz, J., Romeo, I., 2021. Subsurface geometry and emplacement conditions of a giant dike system in Elysium fossae, Mars. J. Geophys. Res.: Planets 126, 2020JE006512. https://doi.org/10.1029/2020JE006512.

Rivas-Dorado, S., Ruíz, J., Romeo, I., 2022. Giant dikes and dike-induced seismicity in a weak crust underneath Cerberus Fossae, Mars. Earth Planet Sci. Lett. 594, 117692 https://doi.org/10.1016/j.epsl.2022.117692.

Roberts, G.P., Crawford, I.A., Peacock, D., Vetterlein, J., Parfitt, E., Bishop, L., 2007. Possible evidence for on-going volcanism on Mars as suggested by thin, elliptical sheets of low-albedo particulate material around pits and fissures close to Cerberus Fossae. Earth Moon Planets 101, 1–16. https://doi.org/10.1007/s11038-007-9140-z.

Rubin, A.M., 1995. Propagation of magma-filled cracks. Annu. Rev. Earth Planet Sci. 23, 287–336. https://doi.org/10.1146/annurev.ea.23.050195.001443.

Rubin, A.M., 1992. Dike-induced faulting and graben subsidence in volcanic rift zones. J. Geophys. Res. Solid Earth 97, 1839–1858. https://doi.org/10.1029/91JB02170.

Rubin, A.M., Pollard, D.D., 1988. Dike-induced faulting in rift zones of Iceland and Afar. Geology 16, 413–417. https://doi.org/10.1130/0091-7613(1988)016%3C0413:DIFIRZ%3E2.3.CO;2.

Rubin, A.M., Pollard, D.D., 1987. Origins of blade-like dikes in volcanic rift zones. In: USGS (Ed.), Volcanism in Hawaii, USGS Professional Paper, vol. 1350, pp. 1449–1470.

Ruch, J., Wang, T., Xu, W., Hensch, M., Jónsson, S., 2016. Oblique rift opening revealed by reoccurring magma injection in central Iceland. Nat. Commun. 7, 1–7. https://doi.org/10.1038/ncomms12352.

Russell, P.S., 2003. Elysium-Utopia flows as mega-lahars: a model of dike intrusion, cryosphere cracking, and water-sediment release. J. Geophys. Res. 108, 1–28. https://doi.org/10.1029/2002je001995.

Scholz, C.H., 2002. The Mechanics of Earthquakes and Faulting, second ed. Cambridge University Press, Cambridge. https://doi.org/10.1017/CBO9780511818516.

Schultz, R.A., 2019. Geologic Fracture Mechanics. Cambridge University Press, Cambridge. https://doi.org/10.1017/9781316996737.

Schultz, R.A., 1995. Limits on strength and deformation properties of jointed basaltic rock masses. Rock Mech. Rock Eng. 28, 15.

Schultz, R.A., Lin, J., 2001. Three-dimensional normal faulting models of the Valles Marineris, Mars, and geodynamic implications. J. Geophys. Res. Solid Earth 106, 16549–16566. https://doi.org/10.1029/2001jb000378.

Schultz, R.A., Okubo, C.H., Goudy, C.L., Wilkins, S.J., 2004. Igneous dikes on Mars revealed by Mars orbiter laser altimeter topography. Geology 32, 889–892. https://doi.org/10.1130/G20548.1.

Schultz, R.A., Okubo, C.H., Wilkins, S.J., 2006. Displacement-length scaling relations for faults on the terrestrial planets. J. Struct. Geol. 28, 2182–2193. https://doi.org/10.1016/j.jsg.2006.03.034.

Scott, E.D., 2002. Emplacement of giant radial dikes in the northern Tharsis region of Mars. J. Geophys. Res. 107 https://doi.org/10.1029/2000je001431.

Segall, P., Pollard, D.P., 1983. Nucleation and growth of strike slip faults in granite. J. Geophys. Res. 88, 555–568. https://doi.org/10.1029/JB088iB01p00555.

Sigmundsson, F., Hooper, A., Hreinsdóttir, S., Vogfjörd, K.S., Ófeigsson, B.G., Heimisson, E.R., Dumont, S., Parks, M., Spaans, K., Gudmundsson, G.B., Drouin, V., Árnadóttir, T., Jónsdóttir, K., Gudmundsson, M.T., Högnadóttir, T., Fridriksdóttir, H.M., Hensch, M., Einarsson, P., Magnússon, E., Samsonov, S., Brandsdóttir, B., White, R.S., Ágústsdóttir, T., Greenfield, T., Green, R.G., Hjartardóttir, Á.R., Pedersen, R., Bennett, R.A., Geirsson, H., la Femina, P.C., Björnsson, H., Pálsson, F., Sturkell, E., Bean, C.J., Möllhoff, M., Braiden, A.K., Eibl, E.P.S., 2015. Segmented lateral dyke growth in a rifting event at Bárðarbunga volcanic system, Iceland. Nature 517. https://doi.org/10.1038/nature14111.

Smith, D.E., Zuber, M.T., Neumann, G.A., Guinness, E.A., Slavney, S., 2003a. Mars Global Surveyor Laser Altimeter Mission Experiment Gridded Data Record. MGS-M-MOLA-5-MEGDR-L3-V1.0, NASA Planetary Data System.

Smith, D.E., Zuber, M.T., Neumann, G.A., 2003b. MOLA Precision Experiment Data Record Software Interface Specification (MOLA PEDR SIS) (Greenbelt).

Stähler, S.C., Mittelholz, A., Perrin, C., Kawamura, T., Kim, D., Knapmeyer, M., Zenhäusern, G., Clinton, J., Giardini, D., Lognonné, P., Banerdt, W.B., 2022. Tectonics of Cerberus fossae unveiled by marsquakes. Nat. Astron. 6, 1376–1386. https://doi.org/10.1038/s41550-022-01803-y.

Tanaka, K.L., Chapman, M.G., Scott, D.H., 1992. Geologic Map of the Elysium Region of Mars. ATLAS of MARS 1:5,000,000 GEOLOGIC SERIES. USGS, Denver.

Tanaka, K.L., Robbins, S.J., Fortezzo, C.M., Skinner, J.A., Hare, T.M., 2014. The digital global geologic map of Mars: chronostratigraphic ages, topographic and crater morphologic characteristics, and updated resurfacing history. Planet. Space Sci. 95, 11–24. https://doi.org/10.1016/j.pss.2013.03.006.

Thomas, M.E., Petford, N., Bromhead, E.N., 2004. Volcanic rock-mass properties from Snowdonia and Tenerife: implications for volcano edifice strength. J. Geol. Soc. 161, 939–946. https://doi.org/10.1144/0016-764903-166.

Trippanera, D., Acocella, V., Ruch, J., 2014. Dike-induced contraction along oceanic and continental divergent plate boundaries. Geophys. Res. Lett. 41, 7098–7104. https://doi.org/10.1002/2014GL061570.

Trippanera, D., Ruch, J., Acocella, V., Rivalta, E., 2016. Experiments of dike-induced deformation: insights on the long-term evolution of divergent plate boundaries. J. Geophys. Res. Solid Earth 3782–3803. https://doi.org/10.1002/2015JB012608 (Received).

Trippanera, D., Ruch, J., Passone, L., Jónsson, S., 2019. Structural mapping of dike-induced faulting in harrat lunayyir (Saudi Arabia) by using high resolution drone imagery. Front. Earth Sci. 7, 1–23. https://doi.org/10.3389/feart.2019.00168.

Vaucher, J., Baratoux, D., Mangold, N., Pinet, P., Kurita, K., Grégoire, M., 2009. The volcanic history of central Elysium Planitia: implications for martian magmatism. Icarus 204, 418–442. https://doi.org/10.1016/j.icarus.2009.06.032.

Vaz, D.A., Spagnuolo, M.G., Silvestro, S., 2014. Morphometric and geometric characterization of normal faults on Mars. Earth Planet Sci. Lett. 401, 83–94. https://doi.org/10.1016/j.epsl.2014.05.022.

Walker, R., Stephens, T., Greenfield, C., Gill, S., Healy, D., Poppe, S., 2021. Segment tip geometry of sheet intrusions, I: theory and numerical models for the role of tip shape in controlling propagation pathways. Volcanica 4, 189–201. https://doi.org/10.30909/vol.04.02.189201.

Willemse, E.J.M., Peacock, D.C.P., Aydin, A., 1997. Nucleation and growth of strike-slip faults in limestones from Somerset, U.K. J. Struct. Geol. 19, 1461–1477. https://doi.org/10.1016/S0191-8141(97)00056-4.

Wilson, L., Head, J.W., 2002. Tharsis-radial graben systems as the surface manifestation of plume-related dike intrusion complexes: models and implications. J. Geophys. Res. 107, 5057. https://doi.org/10.1029/2001JE001593.

Wilson, L., Mouginis-Mark, P.J., Tyson, S., Mackown, J., Garbeil, H., 2009. Fissure eruptions in Tharsis, Mars: implications for eruption conditions and magma sources. J. Volcanol. Geoth. Res. 185, 28–46. https://doi.org/10.1016/j.jvolgeores.2009.03.006.

Wright, T.J., Ebinger, C., Biggs, J., Ayele, A., Yirgu, G., Keir, D., Stork, A., 2006. Magma-maintained rift segmentation at continental rupture in the 2005 Afar dyking episode. Nature 442, 291–294. https://doi.org/10.1038/nature04978.

Wyrick, D.Y., Smart, K.J., 2009. Dike-induced deformation and Martian graben systems. J. Volcanol. Geoth. Res. 185, 1–11. https://doi.org/10.1016/j.jvolgeores.2008.11.022.

Xu, W., Jónsson, S., Corbi, F., Rivalta, E., 2016. Graben formation and dike arrest during the 2009 Harrat Lunayyir dike intrusion in Saudi Arabia: insights from InSAR, stress calculations and analog experiments. J. Geophys. Res. Solid Earth 121, 2837–2851. https://doi.org/10.1002/2015JB012505.

Yirgu, G., Ayele, A., Ayalew, D., 2006. Recent seismovolcanic crisis in northern Afar, Ethiopia. Eos 87, 325–329. https://doi.org/10.1029/2006eo330001.